

# The Talbot effect: recent advances in classical optics, nonlinear optics, and quantum optics

Jianming Wen,<sup>1,2,3</sup> Yong Zhang,<sup>1,4</sup> and Min Xiao<sup>1,2,5</sup>

<sup>1</sup>National Laboratory of Solid State Microstructures, School of Physics, College of Engineering and Applied Sciences, Nanjing University, Nanjing 210093, China

<sup>2</sup>Department of Physics, University of Arkansas, Fayetteville, Arkansas 72701, USA

<sup>3</sup>e-mail: jianming.wen@gmail.com

<sup>4</sup>e-mail: zhangyong@nju.edu.cn

<sup>5</sup>e-mail: mxiao@uark.edu

Received November 13, 2012; revised February 25, 2013; accepted February 25, 2013; published March 29, 2013 (Doc. ID 179805)

The Talbot effect, also referred to as self-imaging or lensless imaging, is of the phenomena manifested by a periodic repetition of planar field distributions in certain types of wave fields. This phenomenon is finding applications not only in optics, but also in a variety of research fields, such as acoustics, electron microscopy, plasmonics, x ray, and Bose–Einstein condensates. In optics, self-imaging is being explored particularly in image processing, in the production of spatial-frequency filters, and in optical metrology. In this article, we give an overview of recent advances on the effect from classical optics to nonlinear optics and quantum optics. Throughout this review article there is an effort to clearly present the physical aspects of the self-imaging phenomenon. Mathematical formulations are reduced to the indispensable ones. Readers who prefer strict mathematical treatments should resort to the extensive list of references. Despite the rapid progress on the subject, new ideas and applications of Talbot self-imaging are still expected in the future. © 2013 Optical Society of America

OCIS codes: 070.6760, 050.1970, 110.6760, 260.1960

1. Introduction. . . . .	85
2. Talbot Effect in Classical Optics. . . . .	88
2.1. Basic Theoretical Considerations . . . . .	88
2.2. Advances in Plasmons and Metamaterials . . . . .	91
2.2a. Theoretical Proposals . . . . .	92
2.2b. Experiments on the Plasmon Talbot Effect. . . . .	93
2.2c. Theoretical Proposal on Metamaterials. . . . .	95
2.3. Advances in Waveguides . . . . .	97
2.3a. Multimode Interference Effect . . . . .	97
2.3b. Discrete Talbot Effect. . . . .	99

2.4. Advances in X Ray . . . . .	101
2.4a. Two-Grating Interferometer . . . . .	101
2.4b. Three-Grating Interferometer . . . . .	104
3. Talbot Effect in Nonlinear Optics . . . . .	105
3.1. Integer Second-Harmonic Self-Imaging . . . . .	107
3.2. Fractional Second-Harmonic Self-Imaging . . . . .	108
3.3. Second-Harmonic Talbot Illuminator. . . . .	109
3.4. Enhancement of Two-Wave Mixing . . . . .	110
4. Talbot Effect in Quantum Optics . . . . .	112
4.1. Second-Order Talbot Effect in Quantum Imaging . . . . .	114
4.2. Second-Order Talbot Effect in Quantum Lithography . . . . .	120
4.3. Electromagnetically Induced Talbot Effect. . . . .	122
5. Summary . . . . .	124
Acknowledgments . . . . .	124
References . . . . .	125

# The Talbot effect: recent advances in classical optics, nonlinear optics, and quantum optics

Jianming Wen, Yong Zhang, and Min Xiao

## 1. Introduction

Classical image formation is most commonly associated with some type of lens, with the exception of the earliest means of imaging known to mankind, in which a periodic structure can produce self-images at certain regular distances, as was first discovered by Henry Fox Talbot [1] in 1836. By illuminating a Fraunhofer diffraction grating and a rectangular array of tiny holes with a very small white light source, behind the structures he observed a repetition of alternate color bands of complementary colors (red–green and blue–yellow) resembling the thin slits of the grating themselves at certain distances. About half a century later, in 1881, Lord Rayleigh [2] was the first to prove that this phenomenon is a consequence of the diffraction interference of highly spatially coherent (plane) waves by gratings; the color band structure observed is a manifestation of the periodicity and the shape of the grating. The alternation of complementary color bands occurs at integer multiples of  $z_T = d^2/\lambda$ , called the Talbot distance, where  $d$  and  $\lambda$  are the grating period and the wavelength of the incident plane wave, respectively; bands with equal color patterns thus repeat at integer multiples of  $2z_T$  (the primary Talbot length).

Chronologically, the same phenomenon was later rediscovered by Winkelmann [3], Weisel [4], and Wolfke [5] at the beginning of the last century, as they attempted to understand grating image formation in microscopy. Many years passed until the problem was further revisited by Cowley and Moodie [6–9]. In the mid-1950s, Cowley and Moodie in their pioneering work made an intensive study of the properties of the Fresnel diffraction field behind periodic objects, where they found the grating structure is replicated at multiples of a certain longitudinal distance,  $z_T$ . They termed well-defined object images Fourier images, whereas the intermediate-intensity patterns appearing between Fourier image planes were called Fresnel images. These latter images received much attention in the subsequent work of Rogers [10] and especially Winthrop and Worthington [11]. The terminology “self-imaging” was introduced by Montgomery [12] and has been used together with the term “Talbot effect” in the literature since the 1970s.

In modern language, the Talbot effect is concerned with Fresnel diffraction of a coherent monochromatic wavefront that is (strictly) periodic in the transverse direction. The physics of wave propagation ensures the appearance of strict periodicity along the axis of propagation  $z$ . Montgomery [12] proved lateral periodicity to be a sufficient, but not a necessary, condition for self-imaging. In fact, it is possible to construct signals with a discrete plane-wave spectrum

to exhibit self-imaging not only within the bounds of paraxial optics but also for the nonparaxial domain of propagation.

The invention of affordable coherent light sources gives the Talbot self-imaging new life. Since the 1960s, the simplicity and beauty of the effect has triggered a wave of research related to coherent optical signal processing and resulted in numerous interesting and original applications that provide competitive solutions to various scientific and technological problems. An excellent and comprehensive review article written by Paturski [13] has compiled a detailed survey of the self-imaging phenomenon and its applications to imaging processing and synthesis, photolithography, optical testing, optical metrology, and spectrometry. The survey summarized the progress made in this research area before 1990. Because of the lack of refractive (optical) elements, the effect has also received great attention in the fields of acoustics, x-ray diffraction, electron optics, and electron microscopy. A nice account on these subjects was given by Cowley in his textbook, *Diffraction Physics* [14].

As in optics,  $N$ -slit arrays can be also considered as typical examples of quantum gratings. That is, when such arrays are illuminated with a continuous, coherent wavefront, a continuous quantum flow is observable behind the slits. This flow displays a typical pattern called quantum carpet [15] with periodicity  $d$  along the direction parallel to the plane containing the slits and  $2z_T$  along the propagation direction. Full recurrences are found at integer multiples of  $z_T$ , and these recurrences are the direct analog of the color bands obtained when working with optical gratings. A recurrence that coincides with the initial state describing the diffracted system is called a revival of such a state and appears at integer multiples of  $z_T$ . For even integers, the state appears exactly the same as the initial one, while for odd integers, it is shifted by half a period ( $d/2$ ) with respect to the even-integer case. Recurrences at fractions of  $z_T$  consist of superposed images of the initial state with itself. Indeed, if the boundary conditions of the slits are sharp (or the window function is not differentiable at the edges of the slits), one shall observe fractal structures at irrational fractions of  $z_T$ , which give rise to fractal carpets [16]. Further investigations have revealed that the Talbot effect is far more than a mere optical curiosity, in which much physics still needs to be discovered. On the one hand, the effect is one of a class of phenomena involving the extreme coherent interference of waves. On the other, these phenomena possess deep and unexpected roots in classical number theory. The number-theory properties of the phases in the effect have been proposed as the basis of a means to carry out arithmetic computations through interference. It is the quadratic phases shown in the origin of the Talbot effect that play the key role in revivals and fractional revivals [17], curlicues [18], and Gauss sums [19]. From this point of view, the Talbot process belongs to a broader family of phenomena exhibiting wave packet revivals [20].

The wave nature of matter, most conspicuously revealed in interference studies like the double-slit experiment, is a paradigm of quantum mechanics. Conceptually, the simplest and most palpable matter-wave phenomenon is characterized by far-field diffraction. Yet, the collimation of a molecular beam that is significantly narrower than the diffraction angle brings a great challenge to extend the far-field schemes to objects composed of, say, several hundred thousand atoms. In contrast, near-field phenomena, especially the

Talbot–Lau effect [21], allow one to operate with particle beams of modest coherence, without the need for a spatially resolving particle detector. As such one can draw on favorable length and mass scaling properties. By exploring the Talbot lensless imaging, matter–wave interferences with heavy particles, such as Na<sub>2</sub> molecules [22], Bose–Einstein condensates (BECs) [23], and C<sub>70</sub> fullerene molecules [24], have been experimentally demonstrated. Following Rayleigh’s analysis, the fine detail in Talbot wave functions is also being employed in atom lithography. A noticeable and active research field using Talbot self-imaging with (ultra-)cold atoms/molecules has led to the promising application of atom lithography. For details on this subject, we refer the reader to a very recent review [25].

The well-known duality between the paraxial diffraction of optical beams in space and the temporal distortion of narrowband pulses in dispersion media has been widely explored to propose and create temporal analogs of spatial systems. The temporal counterpart of the Talbot effect occurs as a periodic temporal signal (for instance, a stream of short optical pulses) propagates through a dispersive medium under first-order dispersion conditions. The temporal integer Talbot effect was first described by Jansson and Jansson [26], who proposed using the effect for the transference of information contained in periodic signals along an optical fiber. In that work they found the fiber distances at which an input periodic signal is exactly replicated. Since then the temporal Talbot effect has attracted considerable interest [27–32]. One motivation comes from the fact that the phenomenon is capable of multiplying the repetition rate of periodic pulse sequences without affecting the individual pulse features (such as temporal profile and duration). Generation of optical pulse trains with ultrahigh repetition rate is of great interest for future ultrahigh-rate optical communications and optical computing systems, ultrafast data processing, and other scientific areas.

The scope of self-imaging was dramatically expanded by the study of Fresnel diffraction of periodic signals at rational fractions of the Talbot self-imaging period. Namely, the work by Winthrop and Worthington [11] identified Fresnel images, i.e., the diffraction patterns at so-called fractional Talbot planes, as cases where the Fresnel diffraction integrals can be cast into simple analytic forms. Subsequent investigations further simplified the analytic expressions, culminating either in a discrete matrix formulation [33–35] of near-field diffraction (which relates the amplitudes of sampled periodic signals in different fractional Talbot planes via linear transformations [36–38]) or in a reciprocal vector theory [39,40]. Interest in studying the fractional Talbot effect was greatly increased by the invention of the Talbot array illuminator [41–44], a diffractive optical element to convert a homogeneous wavefront to an array of high equal-intensity spots. Such a device is a phase grating that, under coherent plane-wave illumination, gives rise to 100% modulated, square-wave fields and irradiance patterns solely through Fresnel diffraction. Talbot array illuminators are well suitable to serve as optical interconnects because they are near 100% efficient and are easier to design and fabricate than other interconnection methods, say, Dammann gratings. Another interesting formulation on self-imaging is developed in phase space through, namely, the Wigner distribution function. Self-imaging in phase space was first studied by Ojeda-Castaneda and Sicro [45], who considered both the Talbot effect and the Lau effect. The phase-space analysis was later extended to include the fractional Talbot effect [46] and the design of Talbot array

illuminators [44]. A good account of the subject is a review by Testorf *et al.* in [47].

Work on the Talbot effect is indeed very diverse and has resulted in a long list of publications that run the gamut from reports of its experimental realizations, to discussions of its fundamental physics, to suggestions for implementation variations dictated by practical considerations. Let us begin our review by summarizing its recent advances in classical optics, nonlinear optics, and quantum optics. The present review focuses on the “light optics” Talbot effect, a process in which the object is inserted into a light beam. It can be of an amplitude or phase type or, in general, have a complex amplitude transmittance. This approach, which requires an object at the initial plane, might seem to restrict the scope of these considerations, since some other phenomena exploiting or closely related to self-imaging cannot be treated directly in this way. These include the self-image phenomena in waveguides [48–52] and the general problem of spatial periodicities of light fields [53,54].

Our goal is to provide a compact overview of the fundamentals of optical Talbot self-imaging, using Fourier optics [55] as the framework for analysis and comparison. We begin, in Section 2, by establishing theoretical and new applicational aspects of the Talbot effect in the conventional configuration, that is, the property of the Fresnel diffraction field of some objects illuminated by a spatially coherent light beam. The paraxial approximation is assumed in most of the cases. In reviewing recent progress on self-imaging in classical optics, we focus on new proposals and demonstrations with plasmons, metamaterials, waveguides, and x rays. Theoretical analysis on the effect in waveguides follows the guided-mode propagation model.

Section 3 is devoted to recent observations of self-imaging in nonlinear optics. They are summarized in four groups, namely, the integer nonlinear Talbot effect, the fractional nonlinear Talbot effect, the nonlinear Talbot array illuminator, and enhancement of two-wave mixing (TWM) in photorefractive materials.

In Section 4 the applications of the Talbot effect in quantum optics are described. In comparison with previous sections in which the measurements are involved only with first-order optical coherence, this section introduces the second-order Talbot effect, where self-images are formed from second-order correlation measurements. In particular, we consider the Talbot effect with entangled photon pairs and review the phenomenon in the configurations of quantum ghost imaging and quantum lithography from both the theoretical and experimental viewpoints. In addition, we introduce a recent proposal of imaging (ultra-)cold atoms/molecules with the electromagnetically induced Talbot effect.

Finally, we conclude our review with a very brief summary in Section 5.

## 2. Talbot Effect in Classical Optics

### 2.1. Basic Theoretical Considerations

The Talbot effect, also referred to as self-imaging or lensless imaging, was originally discovered by Talbot more than 170 years ago [1]. Over the years, investigators have come to understand different aspects of this phenomenon, and a theory of the Talbot effect based upon classical diffraction theory [2,6–13] has

emerged that is capable of explaining various observations. Since many of the standard optics textbooks do not even mention the effect, it is worthwhile to bring to the reader's attention the essential features of this fascinating phenomenon.

As mentioned in Section 1, the effect is observed when, under appropriate conditions, a beam of light is reflected from (or transmitted through) a periodic pattern. The pattern may have one-dimensional (1D) periodicity (as in traditional gratings), or it may exhibit two-dimensional (2D) periodicity (e.g., a regular lattice). For simplicity, we choose a 1D periodic object to illustrate the effect. A typical setup of observing the effect is schematically depicted in Fig. 1, where an infinitely extended grating is illuminated with a monochromatic, coherent plane wave of wavelength  $\lambda$ . In Fourier optics, such an object can be represented as

$$A(x) = \sum_{n=-\infty}^{\infty} c_n e^{\frac{2i\pi nx}{d}}, \quad (1)$$

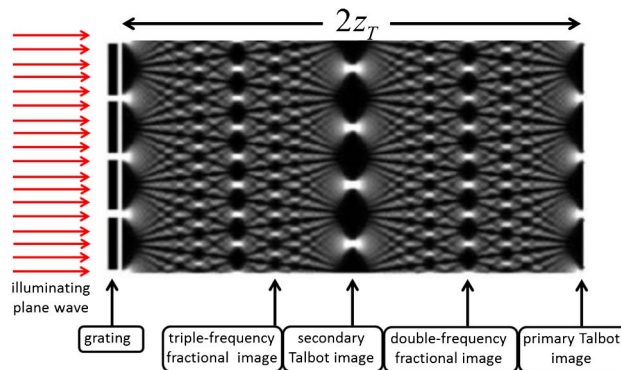
where  $d$  is the spatial period and  $c_n$  is the amplitude of the  $n$ th harmonic. Without specifying the detailed form of Fourier coefficient  $c_n$ , the present analysis is suitable for any type of periodic object.

According to the Fresnel–Kirchhoff diffraction theory [55], the diffracted field amplitude  $E(X)$  is defined in terms of the amplitude transmission of the object  $A(x)$  and the coherent amplitude of the source  $S(x_s)$ . Here,  $X, x, x_s$  are Cartesian coordinates in the observation, object, and source planes, respectively. In the paraxial approximation, the diffracted amplitude  $E(X)$  takes the form of

$$E(X) = \frac{e^{\frac{2i\pi(z_1+z_2)}{\lambda}}}{i\lambda z_1 z_2} \int dx_s S(x_s) \int dx A(x) e^{i\frac{\pi(x-x_s)^2}{\lambda z_1}} e^{i\frac{\pi(X-x)^2}{\lambda z_2}}, \quad (2)$$

where  $z_1$  is the propagation distance between the object and the source, and  $z_2$  the distance from the object to the observation plane. For a plane-wave

Figure 1



The optical Talbot effect for a monochromatic light, shown as a “Talbot carpet.” On the left of the figure the light can be seen diffracting through a grating, and this exact pattern is reproduced on the right of the picture (one Talbot length away from the grating). Halfway between each edge and the middle, one sees the image shifted to the side, and at regular fractions of the Talbot length the sub-images are clearly seen.



illumination, the diffraction amplitude  $E(X)$  at a distance  $z$  from the object is proportional to

$$E(x) \propto \int_{-\infty}^{\infty} dx A(x) e^{i\frac{\pi}{\lambda} \left( z + \frac{x^2}{2z} - \frac{xX}{z} + \frac{X^2}{2z} \right)}. \quad (3)$$

The integration is performed over the infinite boundary on the object plane. Substituting Eq. (1) into Eq. (3) yields

$$E(X) \propto \sum_{n=-\infty}^{\infty} c_n e^{-i\frac{\pi\lambda n^2 z}{d^2}} e^{i\frac{2\pi n X}{d}}. \quad (4)$$

The first exponential term is called the localization term [13], since it states the phase changes of the diffraction orders with the axial distance  $z$ . At a certain distance  $z$ , all diffraction orders are in phase and reinforced by satisfying the condition

$$z = 2m \frac{d^2}{\lambda}, \quad (5)$$

where  $m$ , a positive integer, is referred to as the self-imaging number. In these planes, the Fresnel diffraction images with maximum contrast are constructed and the object function is reproduced. These images are also called Fourier (self-)images by Cowley and Moodie [6–9]. Note that the factor of 2 in Eq. (5) can be omitted. As such, when  $m$  is an odd integer, we can speak about object images with half a period lateral shift with respect to the object. These images result from the  $\pi$  phase shift of odd-number diffraction orders with respect to the zero- and even-order number orders. Now, for  $m = 1$ ,  $z_T = d^2/\lambda$  is the Talbot length for the secondary Talbot image, and  $2z_T$  is for observing the primary Talbot image; see Fig. 1. The fractional Talbot images appear at all rational multiples of  $z_T$ , namely,  $z = (p/q)z_T$ , where  $p$  and  $q$  are coprime integers. Within each unit cell of the imaging plane, these fractional Talbot images consist of  $q$  equally spaced copies of the transmission function of the grating, which superpose coherently as they overlap. In Fig. 1, as an example we mark the fractional Talbot images at distances of  $z_T/3$  and  $3z_T/2$ . The second exponential term in Eq. (4) tells the lateral magnification  $M$  of the diffraction patterns, which is 1 for the plane-wave illumination.

For a Gaussian beam illumination, the condition for the occurrence of the self-imaging becomes

$$z_G = 2m \frac{d^2}{\lambda} \left( \frac{w_z}{w_0} \right)^2, \quad (6)$$

where  $w_0$  denotes the initial waist radius and  $w_z = w_0 \sqrt{1 + (\lambda z / \pi w_0^2)^2}$  is the Gaussian beam radius at the observation plane. The lateral magnification  $M_G$  is

$$M_G = \left( \frac{w_z}{w_0} \right)^2. \quad (7)$$

As seen from Eq. (7) the fundamental difference between self-images under uniform and Gaussian beam illumination is that, in the latter case, there exists a lateral magnification due to the properties of the Gaussian beam. Equations (6)



and (7) tell that, under Gaussian beam approximation, the Talbot lengths and the lateral magnification are  $z$  dependent, and they are not a linear function of  $z$ .

The applications of the Talbot effect are very diverse. Besides the applications described in Section 1, the effect has also been explored to build the Talbot cavity for the coherent combining of output from multiple laser diodes arranged in an array. It is generally constructed with a single mirror at half the Talbot distance from the output facet of the laser array. This images the near-field image of the array back onto the array itself at the primary Talbot distance, creating optical feedback. As such, the feedback forces the diode lasers in the array to mode lock. Laser Talbot cavities, which permit phase locking of laser arrays, are particularly useful for semiconductor lasers [56–58]. We also notice that there is extensive research on grating interferometry in the literature. Since Paturski in his 1989 work [13] gave an excellent review on that, we decide not to repeat it here. Interested readers please refer to [13] and the references therein.

An emerging and interesting alternative to Fourier optics is phase-space optics. Forged by the marriage of joint time–frequency analysis and the phase-space formalism of quantum mechanics, phase-space optics is a platform for describing ray optics, radiometry, coherent Fourier optics, and coherence theory with a single consistent framework. Since the pioneering work by Ojeda-Castaneda and Sircé [45], theoretical analysis on self-imaging in phase space has been extensively addressed through the Wigner distribution function in the literature (for a review, see [47]). We remark here that not all optical phenomena find a natural interpretation in phase space. Due to the strict periodicity of the signals and the discreteness of the Wigner distribution function at its coordinates, however, self-imaging is exceptionally well suited to be analyzed in phase space. The use of phase-space optics not only gives a quantitative analysis but also provides another qualitative and intuitive interpretation on the phenomenon. Since this phase-space formulation is different from the treatments used in this article, we suggest that interested readers refer to the literature for details on the subject.

## 2.2. Advances in Plasmons and Metamaterials

Surface plasmons (SPs) are coherent electron oscillations that are formed at the interface between any two materials where the real part of the dielectric function changes sign across the interface (e.g., a metal sheet in air). SPs have lower energy than bulk (or volume) plasmons, which quantize the longitudinal electron oscillations about positive ion cores within the bulk of an electron gas (or plasma). When SPs are coupled with a photon, the resulting hybridized excitation is called a surface plasmon polariton (SPP). This SPP can propagate along the surface of a metal until its energy is dissipated via absorption in the metal or radiation into free space. Recent research shows that SPPs are also capable of realizing the Talbot effect. Prompted by advanced nanofabrication technologies, although the research on the plasmon Talbot effect started only a few years ago, it has already generated many interesting results. Theoretical proposals on observing plasmon self-imaging are made with metallic/dielectric materials associated with drilled holes, metallic dots, dielectric dots, and metal waveguide arrays [52,59–61]. The first experimental demonstration of the plasmon Talbot effect was performed with a gold grating [62]. Later, the plasmon Talbot effect was observed with the use of Au cylindrical nanostructures [63].

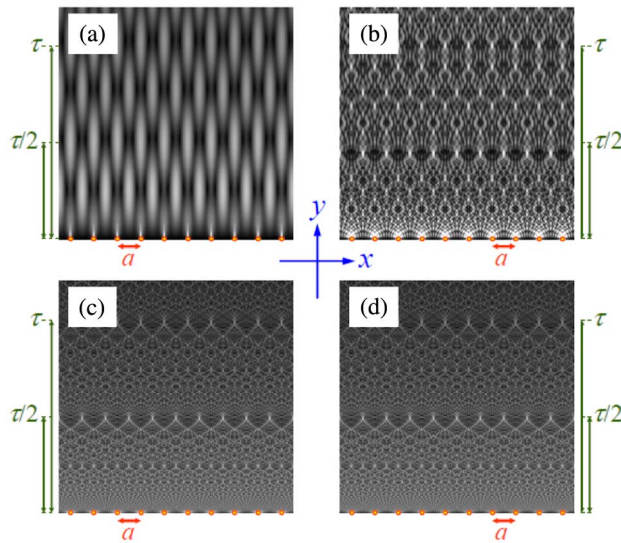
## 2.2a. Theoretical Proposals

The concept of the plasmon Talbot effect was first suggested by Dennis with his colleagues in 2007 [59]. The analog of the Talbot effect using SPs can be made as follows. Suppose a plane-wave light is incident from the back of a metal film, planar except for a periodic one-dimensional array of nanoholes or other sub-wavelength structures with a period  $d$ . The light is partially converted into plasmons on the exit surface of the film and generates a complex carpet pattern. To compute the complex pattern, the field from each nanohole is considered as a dipole, oscillating with a frequency corresponding to the incident light with a wavelength  $\lambda$ . The oscillation drives SPs with a propagating wavelength  $\lambda_{\text{SP}} = \lambda / \text{Real}[\sqrt{\epsilon/(1+\epsilon)}]$ , where  $\epsilon$  is a frequency-dependent dielectric function of the metal. The ideal plasmon Talbot field comes from an infinite sum of single dipole fields. Mathematical calculations [59] give the Talbot length as  $z_T = d^2/\lambda_{\text{SP}}$ . Their numerical simulations indicate that the plasmon Talbot carpet can be clearly observed when  $d \gg \lambda_{\text{SP}}$ , as shown in Fig. 2.

In 2009 Maradudin and Leskova [60] further theoretically analyzed the SPPs scattered by a row of metallic or dielectric dots deposited on a planar silver substrate. On the basis of an impedance boundary condition, their numerical simulations revealed that the transmitted field displayed self-imaging of the rows of dots when the period of the structure was much larger than the plasmon wavelength, a similar condition first addressed in [59]. As illustrated in Figs. 3(b) and 3(c), plasmon Talbot carpets are well developed on a silver surface with a row of silicon dots with a spacing period  $b = 10\lambda_{\text{SP}}$  and  $b = 20\lambda_{\text{SP}}$ , respectively. However, for  $b = \lambda_{\text{SP}}$ , only periodic intensity patterns are formed.

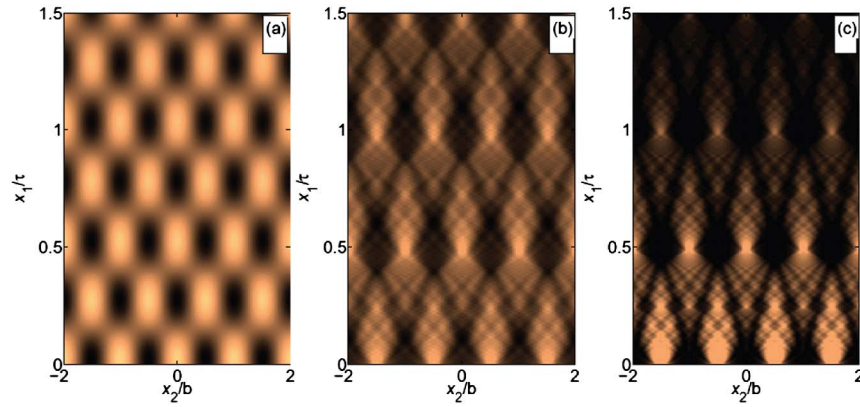
Based upon the mode solutions for homogeneous media, Niconoff *et al.* [61] developed a more general treatment to describe the SPP modes and applied

Figure 2



Plasmon Talbot carpets for a metal film drilled by an array of nanoholes with different periods  $a$ : (a)  $a = \lambda_{\text{SP}}$ , (b)  $a = 5\lambda_{\text{SP}}$ , and (c) and (d)  $a = 20\lambda_{\text{SP}}$ . As one can see, the Talbot effect is not yet developed in (a). For larger periodicities, as in (b)–(d), Talbot self-images are clearly observable. Reproduced with permission, © 2007. Optical Society of America [59].

Figure 3



Plasmon Talbot effect formed by SPPs propagating along a silver surface and scattered by a row of silicon dots with periods of (a)  $b = \lambda_{SP}$ , (b)  $b = 10\lambda_{SP}$ , and (c)  $b = 20\lambda_{SP}$ . Reprinted by permission from IOP publishing Ltd: [60], 2009.

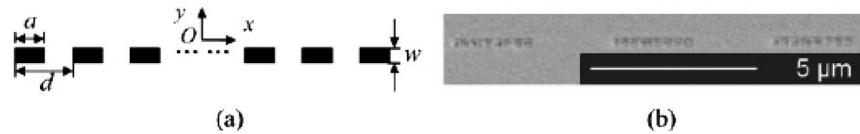
it to analyze the plasmon Talbot self-imaging. Another interesting proposal was made about the discrete plasmonic Talbot effect in metal waveguide arrays [52]. We shall discuss this work in detail in Subsection 2.3.

### 2.2b. Experiments on the Plasmon Talbot Effect

The first plasmon self-imaging experiment [62] was performed by Zhang and his coauthors using SPP launching gratings (SPPLGs). Figure 4(a) illustrates the schematic of the SPPLG, which is composed of periodic grooves located on a gold film with length  $a$ , width  $w$ , and period  $d$ . The figure of merit to quantify the SPPLG is defined by the “opening” ratio,  $\alpha = a/d$ . In the experiment in [62], a  $y$ -polarized laser beam normally illuminated the SPPLG, and the SPPs were launched at the grooves by deploying a Talbot carpet. The SPPLGs were fabricated by a focused ion-beam milling system on a 50 nm thin gold film thermally evaporated onto a glass substrate. The exciting wavelength was 830 nm, which led to an SPP wavelength of 814 nm. Figure 4(b) shows part of the scanning electron micrograph of the SPPLG with  $d = 6\lambda_{SP}$  and  $\alpha = 1/2$ . The Talbot carpets were detected by a leakage radiation microscopy (LRM) system.

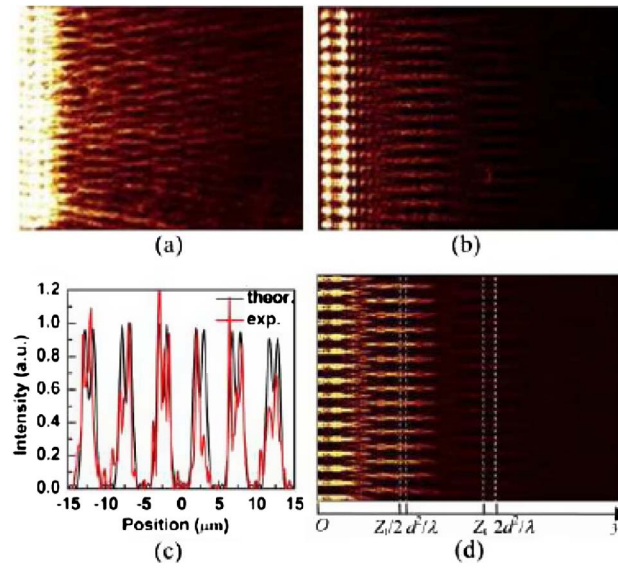
In the experiment, the researchers fabricated two SPPLGs with periods of  $3\lambda_{SP}$  and  $6\lambda_{SP}$ , and the numbers of periods were 20 and 16, respectively. The opening ratios were set as the same,  $\alpha = 1/2$ . The experimental results are shown in Figs. 5(a) and 5(b), respectively. It is obvious to see that the transversal and

Figure 4



(a) Schematic of the SPPLGs. (b) Scanning electron micrograph of the SPPLG with period  $d = 6\lambda_{SP}$  and  $\alpha = 1/2$ . Reproduced with permission, © 2009. Optical Society of America [62].

Figure 5



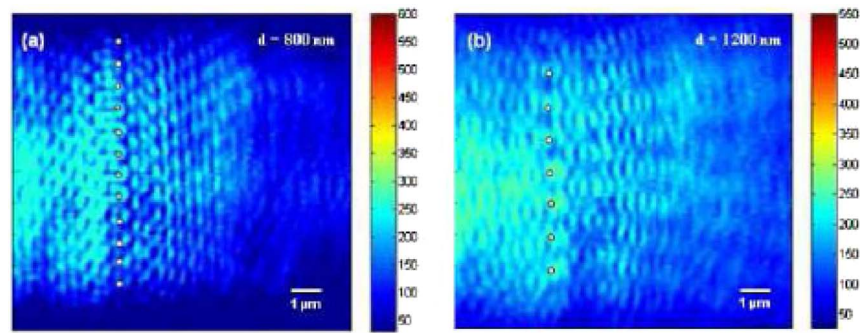
The first experimental demonstration of plasmon Talbot carpets for the SPPLGs with  $d = 3\lambda_{SP}$  (a) and  $d = 6\lambda_{SP}$  (b), respectively. (c) Experimental and theoretical spatial intensity profiles at  $z_t/2$  for the SPPLG with  $d = 6\lambda_{SP}$ . (d) Theoretical Talbot carpet for the SPPLG with  $d = 6\lambda_{SP}$ ; white dashed lines from left to right indicate the positions of  $z_t/2$ ,  $d^2/\lambda$ ,  $z_t$ , and  $2d^2/\lambda$ , respectively. Reproduced with permission, © 2009. Optical Society of America [62].

longitudinal intensity patterns are periodic in Figs. 5(a) and 5(b). Since the periods are compatible with the incident light wavelength, the paraxial approximation is no longer applicable in such a case. The repeating length of the  $\pm n$ th-order beams of the diffracted SPPs is characterized by

$$z_n = \lambda_{SP} / \left( 1 - \sqrt{1 - (n\lambda_{SP}/d)^2} \right), \quad n = 1, 2, 3, \dots \quad (8)$$

For the SPPLG with  $d = 3\lambda_{SP}$  and  $\alpha = 1/2$ , only the 0th- and  $\pm 1$ st-order beams can propagate to the far-field region. Thus, the longitudinal period is determined by the repeating length of the  $\pm 1$ st-order beams,  $z_1 = 17.5\lambda_{SP} = 14.2 \mu\text{m}$ , which coincides with the experimental result of  $14.2 \mu\text{m}$  obtained by the Fourier transformation of the longitudinal intensity distribution in Fig. 5(a). In the case of  $d = 6\lambda_{SP}$  and  $\alpha = 1/2$ , the 0th-,  $\pm 1$ st-,  $\pm 3$ rd-, and  $\pm 5$ th-order beams can all be observed in the far field. These repeating lengths do not generally coincide with each other. In the experiment, Zhang *et al.* measured the Talbot distance  $z_t = 30z_5 = 54.6 \mu\text{m}$ , close to  $9z_3 = 54.6 \mu\text{m}$  and  $z_1 = 58.2 \mu\text{m}$ . Figure 5(c) illustrates the experimental spatial intensity profile of Fig. 5(b) at  $z_t/2$ . Figure 5(d) is the numerically computed Talbot carpet corresponding to the case in Fig. 5(b), which matches well with their experimental result. The four dashed lines from left to right in Fig. 5(d) indicate the positions of  $z_t/2$ ,  $d^2/\lambda$ ,  $z_t$ , and  $2d^2/\lambda$ , respectively. We should remark that the paraxial approximation is also invalid in the current case. Figure 5(c) shows a good agreement between the experimental and theoretical intensity profiles at  $z_t/2$ .

Figure 6



Experimental demonstration of plasmonic Talbot carpets for Au cylindrical particles with periods of (a) 800 nm and (b) 1200 nm. The small white circles indicate the positions of the Au particles. The incident light with a wavelength of 790 nm traverses from left to right. The reflection of the SPP from the nanostructures creates high-intensity regions that saturate the image on the reflection side. Reproduced with permission, © 2009. Optical Society of America [63].

A similar plasmonic Talbot carpet experiment was independently implemented by Cherukulappurath *et al.* in a row of Au cylindrical particles [63]. In their experiment, the incident SPP propagated toward the nanoparticle array from the left toward the right. Part of the light was transmitted through the nanostructures, while the rest was reflected toward the incidence direction. The left side of the array exhibited certain high-intensity regions due to the interference of the incident and the reflected SPPs. The white dashed lines represented the approximate positions of the nanostructures. The near-field interaction of different diffraction orders created a complex Talbot pattern close to the structures; see Fig. 6. The Talbot pattern developed to several micrometers away from the nanostructures and eventually faded away due to the absorption in the metal. The authors also observed plasmonic hot spots of lateral dimension close to  $\lambda/4$ . Such highly confined focal spots may find applications in nanoscale plasmonic devices.

### 2.2c. Theoretical Proposal on Metamaterials

Metamaterials are artificial materials engineered to have properties that may not be found in nature. With designed periodic patterns, metamaterials are assemblies of multiple individual elements fashioned from conventional microscopic materials, such as metals or plastics. Metamaterials gain their properties not from their composition, but from their artificially designed structures. Their precise shape, geometry, size, orientation, and arrangement affect not only the wavefronts of light or sound in an unconventional manner, but also allow them to possess properties that are impossible with conventional materials. These metamaterials achieve desired effects by incorporating structural elements of sub-wavelength sizes, i.e., features that are actually smaller than the wavelength of the waves they affect.

In a conventional optical material, evanescent waves generally decay exponentially, and hence, no Talbot self-imaging happens if the period of the object is much smaller than the incident wavelength [for example, see Fig. 2(a), where the structure period is equal to the wavelength]. In metamaterials, however, the



situation changes dramatically, since evanescent waves can be converted back to propagating waves and be collected in the far field. Taking advantage of this property, Zhang *et al.* [64] recently theoretically proposed the super Talbot effect in an anisotropic metamaterial, as the period is much smaller than the input wavelength. This type of anisotropic material is called an indefinite metamaterial because the permittivity components have different signs. Unlike the plasmon Talbot effect discussed in the previous subsection, the super Talbot self-imaging is based upon bulk plasmons without diffraction limit.

Because the wavelength  $\lambda_0$  is much larger than the period  $D$ , the paraxial approximation is no longer applicable here. To calculate the Talbot distance, let us consider a 2D indefinite metamaterial, as shown in Fig. 7(a), where a TM plane wave with a wavelength of  $\lambda_0 = 630$  nm propagates along the  $z$  axis. The period of the grating is  $D = 100$  nm, and the duty cycle is 50% (i.e.,  $d = 50$  nm). The light propagation after the input grating structure can be cast in Fourier series as

$$A(x, z) = \sum_n f_n e^{inq_x x} e^{ik_z z}, \quad (9)$$

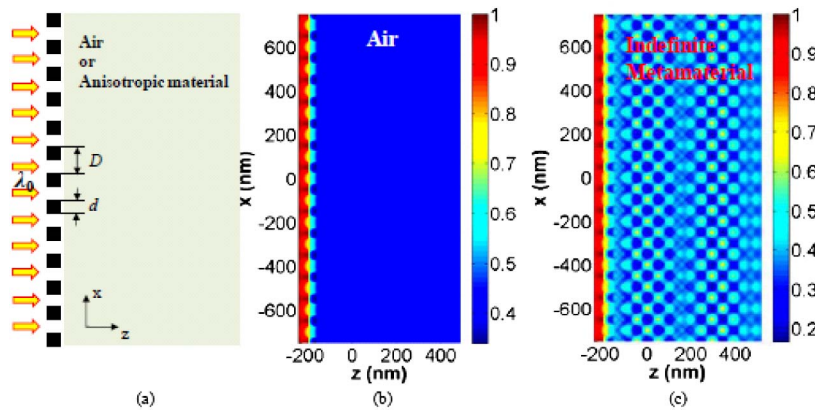
where  $k_x = nq_x = 2n\pi/D$  and  $k_z$  are the wave vectors in transverse direction  $x$  and propagation direction  $z$ , and they obey the dispersion relation

$$\frac{k_z^2}{\epsilon_x} + \frac{k_x^2}{\epsilon_z} = k_0^2, \quad (10)$$

with the wavenumber in free space  $k_0 = 2\pi/\lambda_0$ . Note that Eq. (10) assumes the nonmagnetic material. Plugging Eq. (10) into Eq. (9) yields

$$A(x, z) = \sum_n f_n e^{inq_x x} e^{ik_0 z \sqrt{\epsilon_x \left(1 - \frac{q_x^2}{k_0^2} \epsilon_z\right)}}.$$

Figure 7



(a) Schematic configuration of the Talbot effect in an indefinite metamaterial. The structure period ( $D$ ) is much smaller than the input wavelength,  $\lambda_0$ . (b) No Talbot effect happens using a conventional material under the configuration shown in (a). (c) A Talbot carpet appears in an indefinite metamaterial. Reproduced with permission, © 2011. Optical Society of America [64].

Under the long wavelength approximation,  $\lambda_0 \gg D$ , the above equation can be further simplified as

$$A(x, z) = \sum_n f_n e^{inq_x x} e^{i \frac{2\pi n^2}{D} \sqrt{-\frac{\epsilon_x}{\epsilon_z}} z}. \quad (11)$$

From Eq. (11) it is not difficult to obtain the primary Talbot distance in a 2D indefinite metamaterial,

$$z_T \simeq D \sqrt{-\frac{\epsilon_z}{\epsilon_x}}, \quad (12)$$

which depends only on the permittivity components of the metamaterial and the input object period.

In comparison, Fig. 7(b) gives the case in a conventional material where no Talbot self-imaging is observable. Yet, in an indefinite metamaterial with  $\epsilon_z = -1$  and  $\epsilon_x = 1$  the Talbot carpet appears in Fig. 7(c), which was numerically simulated by using a finite-difference time-domain (FDTD) method.

We remark here that the work in [64] focused on indefinite metamaterials. However, one may apply the theory developed above to analyze other types of metamaterials, such as negative refraction index materials. We leave this problem as an exercise for interested readers.

## 2.3. Advances in Waveguides

The history of the research on the Talbot effect in waveguides could be dated back to the pioneering work by Bryngdahl [65] and Ulrich [48,66]. In the literature, the study of the Talbot effect in waveguides before 2005 was mainly focused on multimode interference (MMI) devices based on self-imaging. The principle and applications of MMI devices have been overviewed by Soldano and Pennings [49]. The recent experimental demonstration on the discrete Talbot effect in waveguide arrays shapes the research direction and opens a door for new applications in integrated optics. In this subsection, we will briefly review the MMI effect and then concentrate on the discrete Talbot effect.

### 2.3a. Multimode Interference Effect

In multimode waveguides, self-imaging due to MMI happens as an input profile is reproduced in single or multiple images at periodic intervals along the propagation direction of the guide. Figure 8 illustrates the evolution of an input field  $\Psi(y, 0)$  along the propagation  $z$  direction in a multimode waveguide. As we can see, under certain conditions, the direct and mirrored single images of  $\Psi(y, 0)$  are formed by interference at distances  $z$  that are, respectively, even and odd multiples of the Talbot length ( $3L_\pi$ ). Here,  $L_\pi$  is the beat length of the two lowest-order modes in the waveguide. Multiple images (or fractional self-images) are formed at rational Talbot lengths. The direct and mirrored single images can be exploited in bar and cross couplers, respectively.

Unlike the Talbot effect in free space, which originates from the periodicity of the input field, the Talbot self-imaging in multimode waveguides is due to the relevance of the propagation constants. To show the mechanism behind this, let



Figure 8

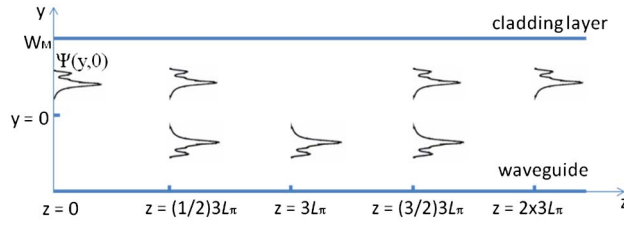


Illustration of the Talbot effect in a multimode waveguide for an input field  $\Psi(y, 0)$ . Along the propagation, one would observe, respectively, a mirrored single image at  $3L_\pi$ , a self-image at  $2 \times 3L_\pi$ , and twofold images at  $3L_\pi/2$  and  $9L_\pi/2$ .

us consider a guided field  $\Psi(y, 0)$  propagating along a step-index multimode ridge waveguide in the  $z$  direction (Fig. 8). The waveguide with width  $W_M$ , ridge refractive index  $n_r$ , and cladding refractive index  $n_c$ , supports  $m$  lateral modes with mode numbers  $v = 0, 1, \dots, m-1$  at a free-space wavelength  $\lambda_0$ . The lateral wavenumber  $k_{yv}$  and the propagation constant  $\beta_v$  are related to the ridge index  $n_r$  through the dispersion equation

$$k_{yv}^2 + \beta_v^2 = k_0^2 n_r^2, \quad (13)$$

with  $k_0 = 2\pi/\lambda_0$  and  $k_{yv} = (v+1)\pi/W_{ev}$ . Here the “effective” width  $W_{ev}$  includes the (polarization-dependent) lateral penetration depth of each mode field and the Goos–Hänchen shifts at the ridge boundaries. For high-contrast waveguides, the penetration depth is usually very small so that  $W_{ev} \simeq W_M$ . In general, the effective widths  $W_{ev}$  can be approximated by the effective width  $W_{e0}$  of the fundamental mode,

$$W_{ev} \simeq W_{e0} = W_M + \frac{\lambda_0}{\pi} \left( \frac{n_c}{n_r} \right)^{2\sigma} \frac{1}{\sqrt{n_r^2 - n_c^2}}, \quad (14)$$

where  $\sigma = 0$  for TE mode and  $\sigma = 1$  for TM. By using the binomial expansion with  $k_{yv} \ll k_0 n_r$ , the propagation constants  $\beta_v$  can be deduced from Eqs. (13) and (14):

$$\beta_v \simeq k_0 n_r - \frac{(v+1)^2 \pi \lambda_0}{4 n_r W_{e0}^2}. \quad (15)$$

Equation (15) shows that the propagation constants in a step-index multimode waveguide are a nearly quadratic function of the mode number  $v$ . By defining the beat of the two lowest-order modes as

$$L_\pi = \frac{\pi}{\beta_0 - \beta_1} \simeq \frac{4 n_r W_{e0}^2}{3 \lambda_0}, \quad (16)$$

the propagation constants spacing can be recast as

$$\beta_0 - \beta_v \simeq \frac{v(v+2)\pi}{3L_\pi}. \quad (17)$$

By following the guided-mode propagation analysis, the input field  $\Psi(y, 0)$  can be decomposed into the modal field distributions  $\psi_v(y)$  of all modes. The field profile at a distance  $z$  can thus be represented as a superposition of all these guided mode field distributions, that is

$$\Psi(y, z) = \sum_{v=0}^{m-1} c_v \psi_v(y) e^{-i\beta_v z}, \quad (18)$$

where  $c_v$  is the excitation coefficient for the  $v$ -th mode. By choosing the phase of the fundamental mode as a common factor out of the sum and dropping it, the field profile  $\Psi(y, z)$  then becomes

$$\Psi(y, z) = \sum_{v=0}^{m-1} c_v \psi_v(y) e^{i(\beta_0 - \beta_v)z} = \sum_{v=0}^{m-1} c_v \psi_v(y) e^{\frac{v(v+2)\pi}{3L_\pi} z}, \quad (19)$$

where Eq. (17) has been applied to derive the second equality. Equation (19) is the essential result for the interpretation of the self-imaging in a multimode waveguide. From the phase term in Eq. (18) it is not difficult to find that, under certain circumstances, the field  $\Psi(y, z)$  will be a replica (or self-image) of the input field  $\Psi(y, 0)$ . For instance, as  $z = p(3L_\pi)$  with  $p$  an integer, direct and mirrored single images of the input field  $\Psi(y, 0)$  are formed at distances  $z$ , as shown in Fig. 8. Many photonic devices based on the MMI effect have been proposed and developed, such as modulators, switches, outcoupling elements of ring lasers, and so on. By exploring the MMI effect in multimode waveguides, a self-imaging silicon Raman amplifier [51] has also been recently proposed.

### 2.3b. Discrete Talbot Effect

In a weakly coupled waveguide array, the discrete Talbot effect has been demonstrated by Iwanow *et al.* in a recent experiment [50]. Thanks to the unique optical properties in discrete systems, the observed discrete Talbot effect exhibits distinguishing characteristics from continuous systems: (1) the Talbot revivals are possible only for a finite set of periodicities, and (2) the Talbot length is independent of the input period but depends on the coupling coefficients of waveguide arrays.

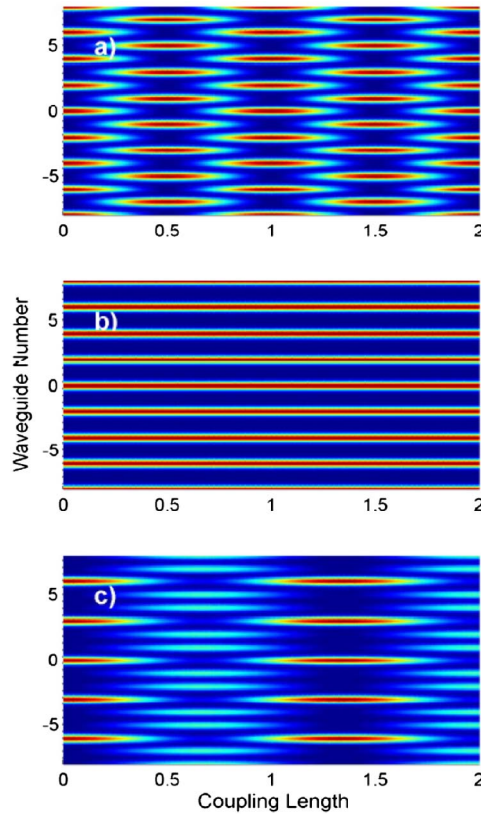
Before we turn to the experiment [50], let us briefly outline the theoretical analysis on the discrete Talbot effect. In an infinite array of weakly coupled discrete elements (such as optical waveguides and coupled microcavities), the modal electric-field amplitudes evolve according to

$$i \frac{dU_n}{dz} + \kappa(U_{n+1} + U_{n-1}) = 0, \quad (20)$$

where  $\kappa$  denotes the coupling coefficient between elements, and  $z$  stands for propagation distance. The solutions of Eq. (20) are periodic Floquet–Bloch-like functions, i.e.,  $U_n = e^{inQ} e^{i\lambda z}$ , where  $Q$  is a phase shift among successive sites and  $\lambda = 2\kappa \cos Q$  is an eigenvalue. To ensure that the Talbot effect takes place, the input field profile should be periodic, and this leads to a periodic boundary condition,  $U_{n+N} = U_n$ , with  $N$  the spatial period of the input. Such a periodic boundary condition requires that  $Q$  take values only from the discrete set  $Q = m\theta$  with  $\theta = 2\pi/N$  and  $m = 0, 1, \dots, N-1$ . Hence, as a result of periodicity, the

field evolution at site  $n$  may be represented by a orthonormal set of functions  $a_n^{(m)} = N^{-1/2} e^{inQ_m} e^{i\lambda_m z}$ , i.e.,  $U_n^{(N)} = \sum_{m=0}^{N-1} c_m a_n^{(m)}$ . It now becomes clear that the field revivals are possible at intervals  $z = 2l\pi/\lambda_i$  (where  $l$  is an integer). To establish the identity,  $\lambda_i/\lambda_j = p/q$  for any two eigenvalues has to be satisfied with  $p$  and  $q$  coprime integers. This further requires that  $\cos(2\pi/N)$  be rational for some  $N$ . With the use of Chebyshev polynomials, after some deductions one can prove that discrete Talbot revivals are possible only for a finite set of periodicities  $N \in \{1, 2, 3, 4, 6\}$ , where  $N = 1$  represents the trivial case of a discrete plane-wave solution. For any other periodicity, the field evolution is nonperiodic. This finding is in contrast to what happens in the continuous Talbot case, where the recurrences are period independent. Of course, for specific periodic inputs it is possible to reveal revivals even when  $N$  does not fall into the set described above. Figure 9 shows the theoretical simulations of the discrete Talbot carpet with different inputs. Figure 9(a) depicts periodic intensity revivals as the binary input is  $\{1, 0, 1, 0, \dots\}$ . The intensity Talbot carpet for this case gives the discrete Talbot distance  $z = \pi/2\kappa$ . If the array is excited at an angle, the binary input is then phase shifted according to  $\{e^{i\phi}, 0, e^{3i\phi}, 0, \dots\}$ . The discrete Talbot period now changes to  $z = \pi/2\kappa \cos \phi$ . As  $\phi \rightarrow \pi/2$ , the Talbot revivals slow down and eventually disappear; see Fig. 9(b). Figure 9(c) gives another Talbot intensity carpet as the input periodic pattern  $\{1, 0, 0, 1, 0, 0, \dots\}$  with a

Figure 9



Discrete Talbot intensity carpets for different input field patterns: (a)  $\{1, 0, 1, 0, \dots\}$ , (b)  $\{1, 0, -1, 0, \dots\}$ , and (c)  $\{1, 0, 0, 1, 0, 0, \dots\}$ . Figure 1 reprinted with permission from R. Iwanow *et al.*, Phys. Rev. Lett. 053902 (2005) [50]. Copyright 2005, the American Physical Society. <http://prl.aps.org/abstract/PRL/v95/i5/e053902>

period  $N = 3$ . In this case, the intensity in the initially excited channels evolves by obeying  $[5 + 4 \cos(3\kappa z)]/9$ , while in the unexcited channels it varies as  $2[1 - \cos(3\kappa z)]/9$ . The Talbot period reads as  $z_T = 2\pi/3\kappa$ .

The experimental demonstration [50] was performed in a channel waveguide array, which was fabricated on a Z-cut LiNbO<sub>3</sub> wafer with use of the standard lithography and Ti indiffusion techniques. The spacing between two neighboring channels was 15  $\mu\text{m}$ . A tunable diode laser was reshaped to be highly elliptical (500  $\mu\text{m} \times 3.5 \mu\text{m}$ ) and was focused by a 10 $\times$  objective onto the input facet of the array sample. Amplitude transmission masks were put in contact with the sample for clean in-phase mode excitation. Because of the sample's excellent linear properties (low scattering), it is very difficult to observe the effect from the top. The indirect observation of the Talbot process at the output of the array was possible by varying the wavelength (and hence the coupling length) over the full spectral range of the laser (1456–1584 nm). This change in coupling strength along with wavelength is, in fact, equivalent to varying the effective sample length. Their experimental results corresponding to the periodic  $\{1, 0, 1, 0, \dots\}$ ,  $\{1, 0, -1, 0, \dots\}$ , and  $\{1, 0, 0, 1, 0, 0, \dots\}$  inputs are, respectively, shown in Figs. 10(a)–10(c). As we can see, the experimental data agrees well with theoretical simulations shown in Figs. 9(a)–9(c).

With the development of plasmonics, Wang with his colleagues proposed to observe the discrete plasmonic Talbot effect in the sub-wavelength metal waveguide arrays [52]. Using PT-symmetric photonic lattices, in a recent theoretical proposal [67] Ramezani *et al.* showed that Talbot self-imaging revivals are possible for input patterns with periodicities dictated by the discreteness of the lattice and the strength of gain and loss parameters.

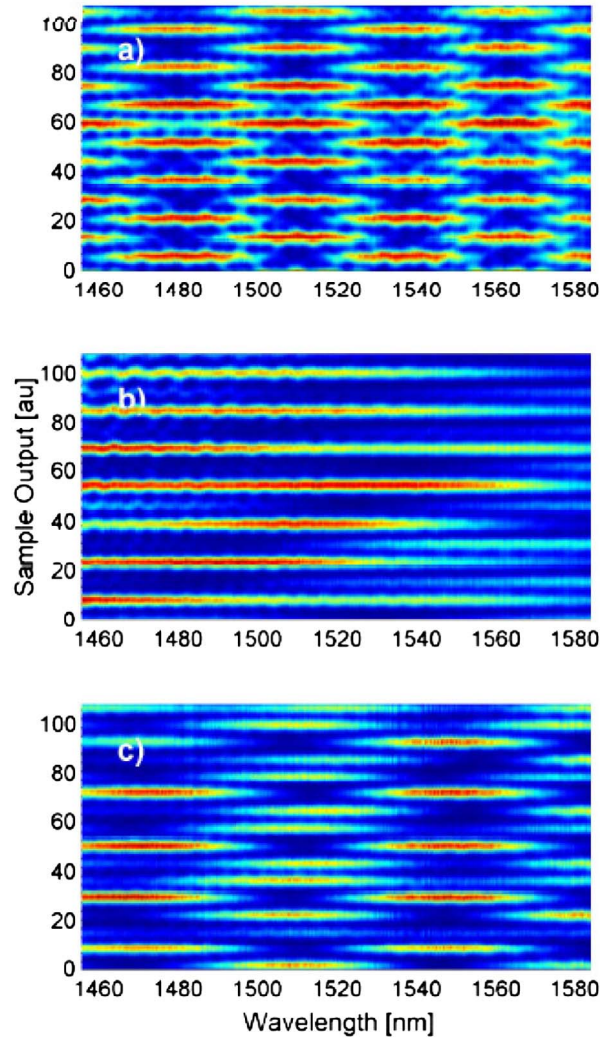
## 2.4. Advances in X Ray

Because of its relatively poor coherence, the realization of x-ray self-imaging turns out to be a challenging task. Despite the lack of effective optics for x rays, lensless Talbot interferometry provides a powerful tool for obtaining high-quality x-ray imaging. With the third-generation synchrotron radiation beams, the first Talbot self-imaging with hard x ray was realized in the  $10^{-11}$  m wavelength range 15 years ago [68]. Recent progress on x-ray phase imaging by grating interferometers has attracted considerable attention in the community. One reason is because the use of gratings as optical elements in hard x-ray phase imaging can overcome problems that so far impair the wider use of phase contrast in x-ray radiography and tomography. In this subsection, we will focus on recent experimental demonstrations on x-ray Talbot interferometers [69–76]. Other work, such as that concerning phase contrast imaging of terahertz photon-polaritons [77] and the electron Talbot interferometer [78], will not be considered here. We suggest that interested readers refer to the references for details.

### 2.4a. Two-Grating Interferometer

As schematically shown in Fig. 11, an x-ray Talbot interferometer typically consists of a phase grating ( $G_1$ ) and an absorption grating ( $G_2$ ). After the first grating  $G_1$ , the incident beam forms a periodic interference fringes in the plane of  $G_2$ . A phase object in the incident beam would induce phase perturbations into the wavefront and lead to displacements of these interference fringes. The absorption grating  $G_2$ , with the same period and orientation as the interference fringes,

Figure 10



Experimental verifications on theoretical discrete Talbot revivals shown in Fig. 9 with input fields of (a)  $\{1, 0, 1, 0, \dots\}$ , (b)  $\{1, 0, -1, 0, \dots\}$ , and (c)  $\{1, 0, 0, 1, 0, 0, \dots\}$ . Figure 4 reprinted with permission from R. Iwanow *et al.*, Phys. Rev. Lett. 053902 (2005) [50]. Copyright 2005, the American Physical Society. <http://prl.aps.org/abstract/PRL/v95/i5/e053902>

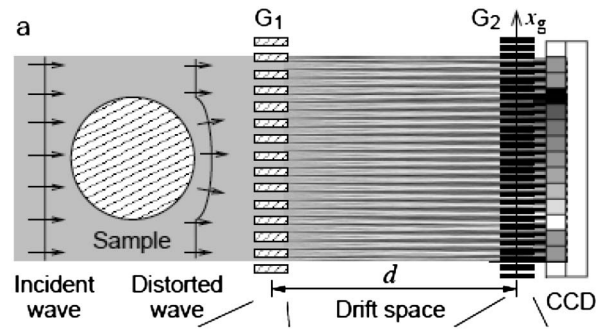
is placed in front of the detector to transform local fringe position into signal intensity variation. By detecting these displacements, one can reconstruct the shape of the wavefront and generate the image. For instance, for a phase grating  $G_1$  with a phase shift of  $\pi$ , the period of  $G_2$  should be half of the period of  $G_1$ . To achieve the maximal contrast, the distance  $d$  between the two gratings should satisfy the condition

$$d_m = \left(m - \frac{1}{2}\right) \frac{p_1^2}{4\lambda}, \quad m = 1, 2, 3, \dots \quad (21)$$

Such a two-grating interferometer has recently become a workhorse for x-ray phase-contrast imaging to yield dark-field scatter images with high quality [69–73]. In these demonstrations, biological samples, polymers, and fiber composites with small refractive indices have been clearly revealed through such an



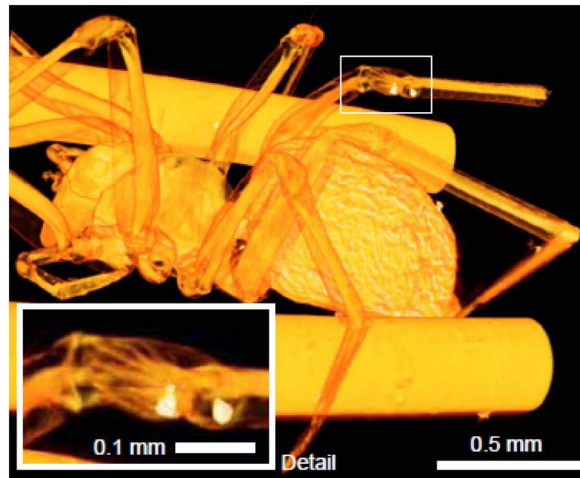
Figure 11



Schematic illustration of grating-based hard x-ray interferometer: The beam splitter grating ( $G_1$ ) splits the incident beam into essentially two diffraction orders, which form a periodic interference pattern in the plane of the analyzer grating ( $G_2$ ). A phase object in the incident beam causes slight refraction and leads to changes of the locally transmitted intensity through the analyzer.  $G_1$  is usually a phase grating with a period of  $p_1$ , and  $G_2$  is an absorption grating with a period of  $p_2$ . The separation between the two gratings is  $d$ . Reproduced with permission, © 2005. Optical Society of America [73].

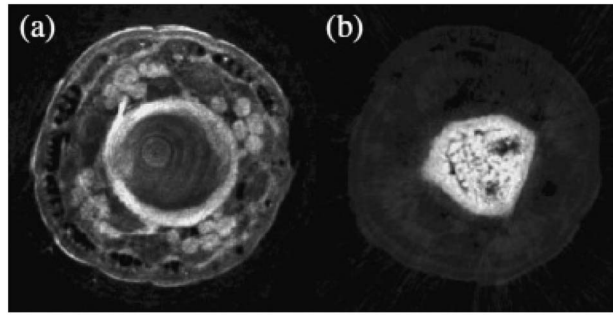
interferometer. As shown in Fig. 12, Pfeiffer with his coauthors [73] obtained details of the internal structure of a small spider that would be difficult to access with other techniques. In this work they achieved spatial resolution of up to a few micrometers. Another interesting experiment led by Momose *et al.* [72] was to image a mouse tail. As shown in Fig. 13, the bones and soft tissues [such as skin, muscle, ligament, and intervertebral disc (cartilage)] are beautifully uncovered in the same view, although with some artifacts in particular caused by the remaining bones. Undoubtedly, these beautiful experiments extend the applications of self-imaging toward medical imaging and bioimaging.

Figure 12



Three-dimensional density-projection rendering of the reconstructed refractive index of a small spider. The parameters of the interferometer are  $p_1 = 4 \mu\text{m}$ ,  $p_2 = 2 \mu\text{m}$ , and  $d = 23.2 \text{ mm}$ . The phase modulation of the phase grating  $G_1$  is  $\pi$ . Reproduced with permission, © 2005. Optical Society of America [73].

Figure 13



Phase tomogram of a mouse tail observed by an x-ray Talbot interferometer with  $p_1 = p_2 = 8 \mu\text{m}$ ,  $\lambda = 0.04 \text{ nm}$ , and  $d = p_1^2/2\lambda$ . In this experiment,  $G_1$  is a  $\pi/2$  phase grating. Copyright 2006. The Japan Society of Applied Physics [72].

### 2.4b. Three-Grating Interferometer

The two-grating Talbot interferometer indeed advances x-ray phase-contrast imaging for medical and industrial applications. However, these applications are still limited due to weak absorption of x ray in biological tissues and polymers. To further enhance the signal-to-noise ratio and image quality, Pfeiffer with his colleagues placed another grating after the x-ray source and set up a three-grating interferometer for low brilliance hard x-ray phase-contrast imaging [75,76].

Figure 14 illustrates the setup configuration of a three-grating x-ray interferometer. In comparison with the two-grating system (Fig. 11), the major difference is that a transmission grating  $G_0$  with a period of  $p_0$  is inserted after the source.  $G_0$  serves as a source grating to create an array of individually coherent but mutually incoherent line sources. The distance between  $G_0$  and  $G_1$  is  $l$ . To ensure the line sources interfere constructively, the following condition must be satisfied:

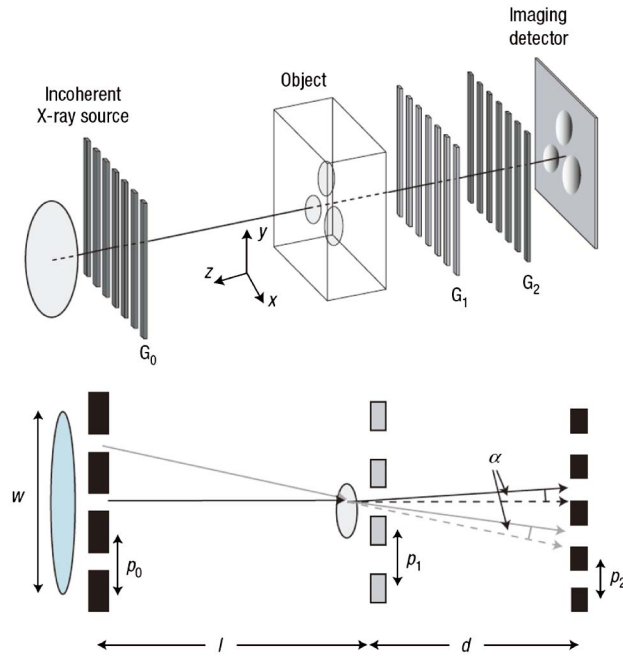
$$p_0 = p_2 \times \frac{l}{d}. \quad (22)$$

The grating  $G_1$  can be either a phase grating or a transmission grating. One advantage of the three-grating interferometer setup is that it allows efficient use of standard x-ray generators with source sizes of more than a square millimeter.

In 2006, Pfeiffer and his colleagues applied the three-grating x-ray interferometer (where  $G_1$  is a transmission grating) to a biological object, a small fish (*Paracheirodon axelrodi*) and performed differential phase-contrast imaging [75]. Their experimental result in comparison with the conventional x-ray transmission image is shown in Fig. 15. Since both images [Figs. 15(a) and 15(b)] were extracted from the same dataset, the total exposure time, and thus the dose delivered to the sample, was identical for the two cases. As expected, the skeleton of the fish and other highly absorbing structures are clearly visible in the conventional radiograph [Figs. 15(a) and 15(e)]. However, the different constituents of the eye are hardly visible in the conventional absorption image shown in Fig. 15(g). In the corresponding differential phase-contrast image [Fig. 15(h)], they are clearly visible. The differential phase-contrast image shown in Fig. 15(f) also reveals complementary details of the soft tissue structure surrounding the otoliths, whereas only the highly absorbing structures are visible in the corresponding transmission image [Fig. 15(e)]. They further



Figure 14



Configuration of a three-grating x-ray interferometer for hard x-ray phase imaging.  $G_0$  and  $G_2$  are absorption gratings with periods of  $p_0$  and  $p_2$ , respectively.  $G_1$  can be a phase grating or a transmission grating, with period of  $p_1$ . The distance between  $G_0$  and  $G_1$  is  $l$  and that between  $G_1$  and  $G_2$  is  $d$ . Reprinted by permission from Macmillan Publishers Ltd: Nat. Phys. 2, 258–261 [75], copyright 2006. [www.nature.com/nphys/](http://www.nature.com/nphys/).

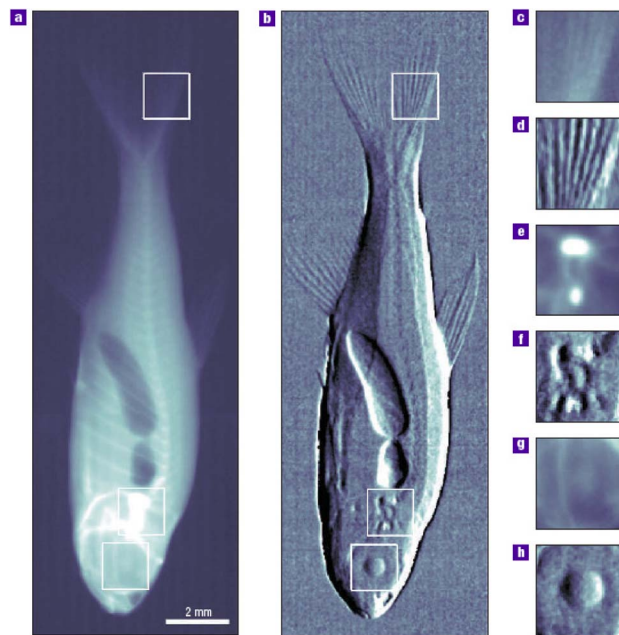
observed that smaller structures with higher spatial frequencies, for example, the fine structure of the tail fin, are better revealed in the differential phase-contrast image [Fig. 15(d)] than in the corresponding absorption radiograph [Fig. 15(c)].

In 2008, the same group implemented another x-ray dark-field scatter imaging by setting up a three-grating interferometer, in which  $G_1$  was a phase grating [76]. In the experiment, they applied the method to a chicken wing and showed the potential for improved contrast in medical imaging. Figure 16(a) gives the conventional transmission contrast and Fig. 16(b) gives the dark-field contrast. By comparing Fig. 16(a) with Fig. 16(b), it is obvious that the boundaries and interfaces produce a stronger signal in the dark-field image. Moreover, from the dark-field image one can clearly see highly porous and strongly scattering microstructures in the chicken bones.

### 3. Talbot Effect in Nonlinear Optics

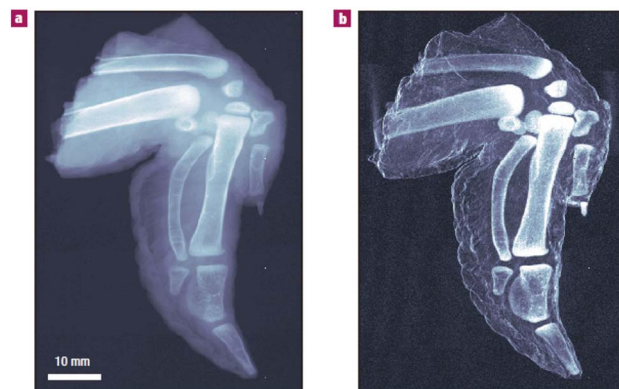
The extension of the Talbot effect to nonlinear optics is relatively new and has not been much explored. Currently, two kinds of nonlinear optical processes are involved with the Talbot effect experimentally: second-harmonic generation (SHG) and two-wave mixing (TWM). The second-harmonic (SH) Talbot effect [79–82] was observed in periodically poled  $\text{LiTaO}_3$  (PPLT) crystals, where the sign of the second-order nonlinear optical coefficients  $\chi^{(2)}$  has a periodic distribution due to the reversal of the ferroelectric domains, i.e.,  $+\chi^{(2)}$  in positive domains and  $-\chi^{(2)}$  in negative domains. Unlike the case in linear optics, the

Figure 15



X-ray images of a small fish obtained with (a) a conventional transmission image and (b) differential phase-contrast imaging. (c)–(h) Two-times magnified and contrast-optimized parts of the transmission [(c), (e), (g)] and the differential phase-contrast image [(d), (f), (h)]. (c) and (d) show parts of the tail fin, (e) and (f) show the region around the otoliths, and (g) and (h) show the eyes of the fish. Reprinted by permission from Macmillan Publishers Ltd: Nat. Phys. 2, 258–261 [75], copyright 2006. [www.nature.com/nphys/](http://www.nature.com/nphys/).

Figure 16



Observation of a chicken wing (a) in a conventional transmission image and (b) in a dark-field image. The x-ray scattering due to the porous microstructure of the bones and the reflection at internal or external interfaces produce a strong signal in the dark-field image. Reprinted by permission from Macmillan Publishers Ltd: Nat. Mater. 7, 134–137 [76], copyright 2008. <http://www.nature.com/nmat/index.html>.

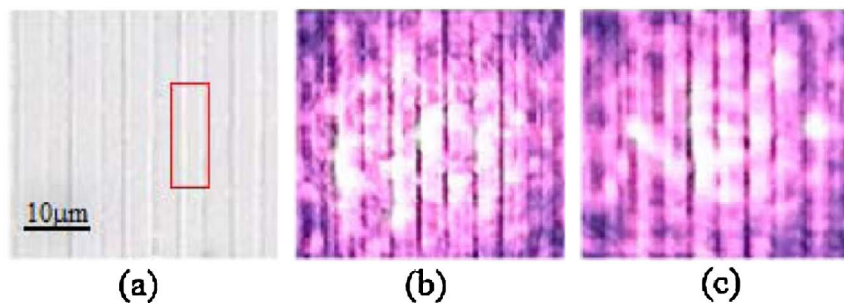
SH Talbot effect presents a self-image of  $\chi^{(2)}$  rather than the refractive index  $n$ . Another effort is made to enhance the TWM gain in a stack of photorefractive liquid crystals valves [83]. Such an enhancement can be attributed to the effect of amplifying the modulation depth of the interference pattern and a phase shift between the refractive index gratings over successive cells. In this section, we will review recent developments in these two different directions.

### 3.1. Integer Second-Harmonic Self-Imaging

PPLT crystals are important nonlinear optical materials because they offer efficient frequency conversion through the quasi-phase-matching technique. In these manmade crystals, the second-order nonlinear coefficients near the domain walls are different from those inside the domains due to the lattice distortion. Therefore, the generated SH pattern at the sample surface possesses the same periodic structure as the domains within the PPLT crystal. The prerequisite condition of the Talbot effect is thus easily satisfied. Compared to the Talbot effect in linear optics, a number of distinct characteristics are revealed in the newly discovered SH Talbot effect. For example, the self-images are produced by the SH waves rather than the fundamental waves, no real grating object is used, and the spatial resolution is improved by a factor of 2 due to frequency doubling.

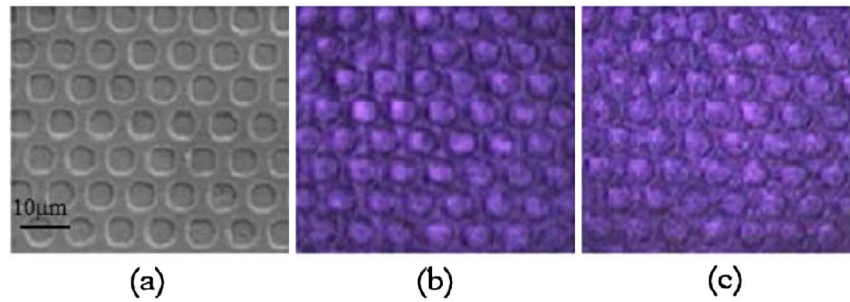
The experiments were performed in 1D and 2D PPLT crystals by Zhang with his colleagues in 2010 [79]. In this experiment, the fundamental input pump laser with a wavelength of 800 nm propagated along the  $z$  axis of the crystals. Figure 17(a) shows the domain structure of the 1D PPLT crystal with a period of 8  $\mu\text{m}$  and a duty cycle of  $\sim 50\%$ . The SH Talbot length for such a 1D structure is calculated to be  $z_T = 4d^2/\lambda_p$ , where  $d$  is the structure period and  $\lambda_p$  the input wavelength. Figures 17(b) and 17(c) are the observed self-images at the first and the third Talbot planes, respectively. The bright SH fringes are generated inside the domains, while the dark lines correspond to the domain walls. The width of the domain wall measured from the images was around 1  $\mu\text{m}$ . The image quality becomes worse at high-order Talbot planes, because of more losses of the diffracted field.

Figure 17



Second-harmonic Talbot effect with a 1D PPLT crystal. (a) The domain structure of the 1D PPLT crystal obtained from SEM. (b) and (c) are the SH self-images recorded at the first and the third Talbot planes, respectively. Figure 2 reprinted with permission from Y. Zhang *et al.*, Phys. Rev. Lett. 183901 (2010) [79]. Copyright 2010, the American Physical Society. <http://link.aps.org/doi/10.1103/PhysRevLett.104.183901>

Figure 18



Second-harmonic Talbot effect with a 2D PPLT crystal. (a) The domain structure. The SH self-images of the 2D PPLT crystal are recorded at the (b) first and (c) third Talbot planes, respectively. Figure 3 reprinted with permission from Y. Zhang *et al.*, Phys. Rev. Lett. 183901 (2010) [79]. Copyright 2010, the American Physical Society. <http://link.aps.org/doi/10.1103/PhysRevLett.104.183901>

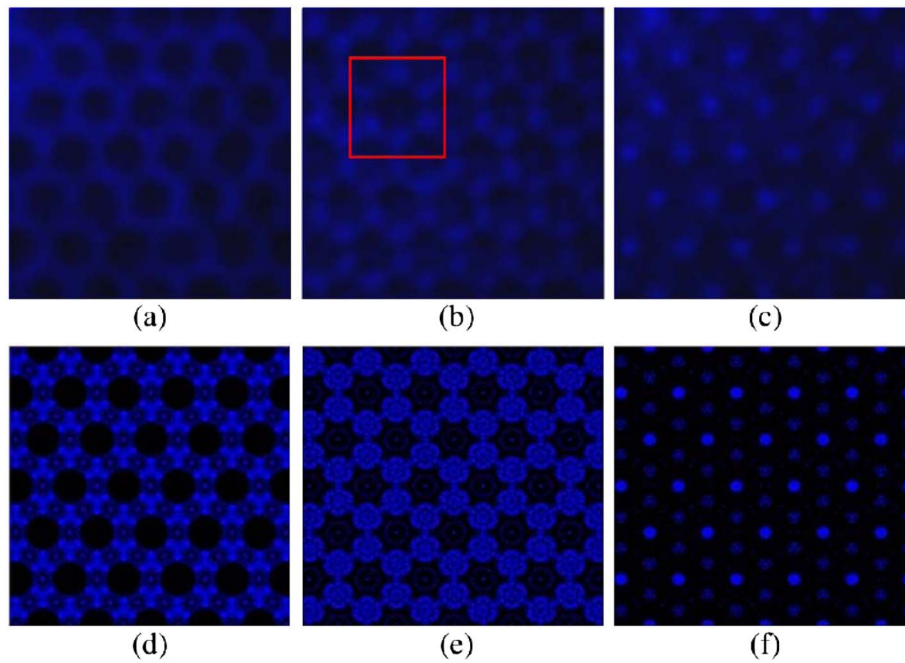
Figure 18(a) shows the structure of a hexagonally poled LiTaO<sub>3</sub> crystal. Its period is 9 μm and the duty cycle is ~30%. The corresponding Talbot length takes the value of  $z_T = 3d^2/\lambda_p$ . Figures 18(b) and 18(c) are the recorded Talbot self-images at the first and the third Talbot planes, respectively.

As pointed out in [79,80], different from the conventional self-images discussed in Section 2, the demonstrated SH Talbot effect is due to the interference of diffracted SH beams in such a way that the periodic intensity patterns of the generated fields at the output surface of the PPLT crystals can be reconstructed after propagating multiples of a certain longitudinal distance. The physics behind this type of nonlinear Talbot effect can be visualized as two consecutive optical processes. The first one is the nonlinear parametric process within the material. In this process, parametric light is produced and because of periodic domain-structure necessity for the phase-matching conditions, the intensity of the generated light follows the same periodicity at the output surface of the material. It is this periodic intensity pattern that forms the “periodic object” for the nonlinear self-imaging. In the first process, since the parametric conversion is a coherent process, the self-images can be used only for imaging the sample surface. From this point, one may argue that it would be difficult to perform 3D imaging with such a nonlinear Talbot effect to examine the whole structure of the sample. However, it is possible to implement 3D imaging by setting up a Talbot interferometer. The second process is the free-space propagation of the generated nonlinear signal. By understanding the physics behind the nonlinear Talbot effect, it is not difficult to conclude that the effect falls into the theoretical analysis presented in Subsection 2.1.

### 3.2. Fractional Second-Harmonic Self-Imaging

The fractional SH Talbot effect was also characterized and reported by Zhang and co-workers [79,81]. By using a 2D PPLT crystal with the same structure described above [see Fig. 18(a)], the fractional self-images at  $1/N$  ( $N = 2, 3$ , and 4) Talbot lengths were experimentally recorded and are shown in Figs. 19(a)–19(c), respectively. In comparison with the integer case shown in Fig. 18, the fractional SH Talbot effect exhibits more interesting and

Figure 19



Fractional SH Talbot images experimentally recorded at (a)  $1/2$ , (b)  $1/3$ , and (c)  $1/4$  Talbot lengths, and (d)–(f) their corresponding theoretical simulations. Reproduced with permission, © (2012). Optical Society of America [81].

complicated features. A  $\pi$  phase shift can be clearly observed in  $1/2$  Talbot planes; see Fig. 19(a). At  $1/3$  Talbot length [Fig. 19(b)], one can clearly see the lattice rotation as well as the period change.

To interpret the observed fractional SH self-imaging, Chen *et al.* [81] applied both the Rayleigh–Sommerfeld diffraction theory and the modified reciprocal vector theory [39,40] to formulate the phenomenon. Their experimental data indicated that the SH background and the duty cycle of the array in the object cannot be ignored. By taking into account these two factors in the theories, their numerical simulations [Figs. 19(d)–19(f)] agree well with the corresponding experimental data [Figs. 19(a)–19(c)].

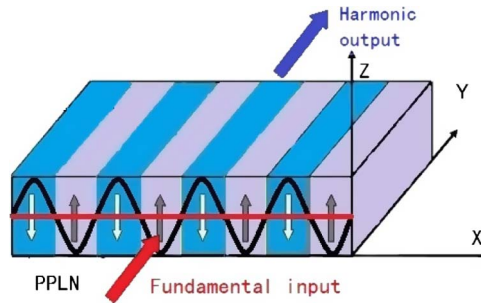
### 3.3. Second-Harmonic Talbot Illuminator

One important application of Talbot self-imaging is to produce a Talbot illuminator (TI) [41–44], which can be used in optical testing, optical computing, and multiple imaging. Very recently, a novel SH TI based on PPLN crystals was proposed by Liu *et al.* through acousto-optic modulation [82]. Because the domain period can be fabricated down to submicrometers and the spatial resolution can be enhanced through frequency doubling, such an SH illuminator may have potential applications in making high-density arrays.

In addition to the excellent nonlinear optical performance, PPLN crystals also have large electro-optic (EO) and acousto-optic (AO) coefficients. An EO tunable phase array based on a PPLN crystal was previously reported by Paturzo *et al.* in 2006 [84]. In this work, no nonlinear optics is involved. Different from [84], however, Liu *et al.* [82] introduced the AO effect into the SH Talbot effect



Figure 20



Schematic diagram of the SH TI, where a driving signal is applied along the  $y$  axis of the crystal. The size of the sample is  $L_x \times L_y \times L_z$ . Reproduced with permission, © 2012. Optical Society of America [82].

to form illuminators. In their theoretical proposal [82], a 1D PPLN crystal of size  $L_x \times L_y \times L_z$  with a period of  $d = 40 \mu\text{m}$  was used. As shown in Fig. 20, the input laser (red arrow) was assumed to be at a wavelength of 800 nm. By applying a radio-frequency field, the PPLN crystal can generate an acoustic standing wave (black curve), which can be resonated inside the crystal or be transduced through a transducer to modulate the phases of the SH waves. For simplicity, their work focused on the resonator case (i.e., the acoustic wave forms a standing wave inside the crystal). The refractive index of PPLN is thus periodically modulated by the acoustic wave. So is the phase of the light traveling through the crystal. The phase shift induced by the acoustic waves is defined by  $\Delta\varphi = (2\pi/\lambda)L_y\Delta n$ .  $\Delta n = n_0^3 P_{21} S_1 / 2$  is the change of the refractive index, where  $n_0$  is the refractive index of the PPLN,  $P_{21}$  represents the involved photoelastic coefficients, and  $S_1$  is the strain due to the acoustic wave along the  $x$  axis. By using the Raman–Nath theory, the maximal amplitude of  $\Delta\varphi$  is [82]

$$\Delta\varphi_m = \frac{\pi}{\lambda} \sqrt{M_2} \sqrt{\frac{2P_s L_y}{L_z}},$$

where  $M_2$  is the acousto-optic figure of merit of the crystal. The power of the acoustic wave  $P_s$  is related to the electromechanical coupling coefficient.

By applying different acoustic powers, the SH pattern can be continuously tuned, as shown in Fig. 21. When the acoustic power is high enough, the SH wave is focused into a series of narrow lines, i.e., the acoustic wave can work as a group of micrometer lenses. More interestingly, if an external acoustic wave is introduced, the 1D SH illuminator can be tuned to 2D (Fig. 22).

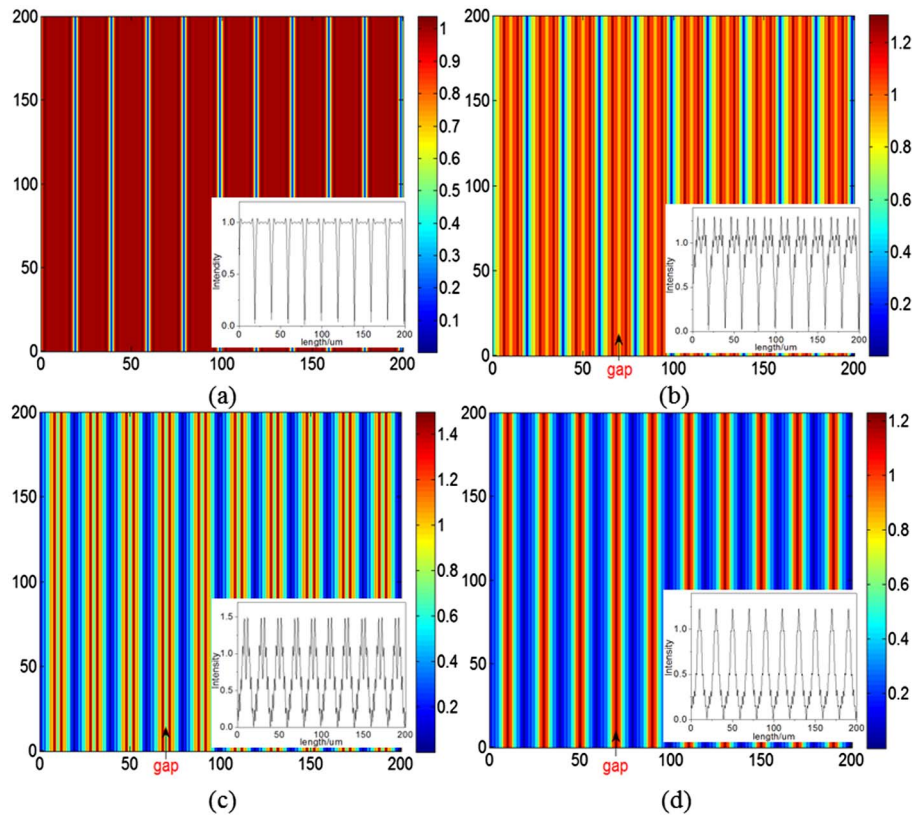
### 3.4. Enhancement of Two-Wave Mixing

Under certain circumstances, TWM (also referred as two-beam coupling) can interact in a photorefractive crystal in such a manner that the energy is transferred from one beam to the other. In the process, the TWM gain is defined as

$$G = |S_{\text{out}}|^2(\text{with the pump}) / |S_{\text{out}}|^2(\text{without the pump}), \quad (23)$$

where  $|S_{\text{out}}|^2$  is the intensity of the output signal. TWM can be used to amplify a weak, image-bearing beam by means of an intense pump beam.

Figure 21



Second-harmonic TI formed from a 1D PPLN crystal works at different acoustic power. (a) 0.10 W, (b) 0.54 W, (c) 0.64 W, and (d) 1.38 W. Reproduced with permission, © 2012. Optical Society of America [82].

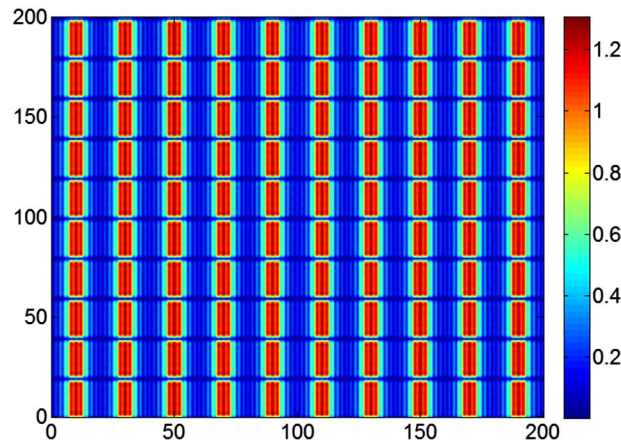
The photorefractive liquid-crystal (LC) light valve is a particularly useful device for realizing high-gain TWM in a thin film. It is a hybrid organic–inorganic cell with the substrates made of a photorefractive crystal, such as  $\text{B}_{12}\text{SiO}_{20}$  (BSO), and a glass plate. The photorefractive crystal acts as a photoconductive medium. When the valve is addressed optically, the BSO crystal permits modulation of the voltage across the LC as a function of light intensity. The typical response time is tens of milliseconds, which is a characteristic of the LC. The TWM in such an LC light valve leads to optical amplification in the Raman–Nath regime of diffraction.

With the help of the Talbot effect, the TWM gain can be further enhanced by use of  $N$  LC light valves [83]. Figure 23 shows a typical experimental setup for TWM with two identical valves ( $N = 2$ ). The first maximum  $G$  occurs at a separation of  $0.75z_T$  between the two valves, and the maximum is recursively obtained at each  $z_T$  distance [Fig. 24(a)]. Here,  $z_T = p^2/\lambda$  is the Talbot length defined as usual with the spatial period of the pattern  $p$  and the incident wavelength  $\lambda$ . Compared with the one-valve configuration, the gain with use of two valves has an enhancement of 2–5 times, as shown in Fig. 24(b).

The gain increase is attributed to the Talbot effect for two reasons. First, as shown in Fig. 25, the Talbot carpet presents amplified interference modulation with the existence of additional light valves. Second, the fractional Talbot effect



Figure 22



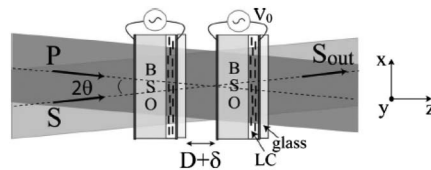
The SH pattern is tuned to 2D when inducing an external acoustic wave (1 W) along the direction perpendicular to the domain walls. Reproduced with permission, © 2012. Optical Society of America [82].

also induces a  $\pi/2$  phase shift between the refractive index gratings over successive cells. This is analogous to the optimized condition in bulk photorefractive crystals, where maximum amplification of the signal intensity occurs when there is  $\pi/2$  phase shift between the interference pattern and the index grating. For the  $N = 3$  case, the maximum  $G$  happens at distances of  $0.88z_T$  between the first two valves and  $0.75z_T$  between the second and third valves.

#### 4. Talbot Effect in Quantum Optics

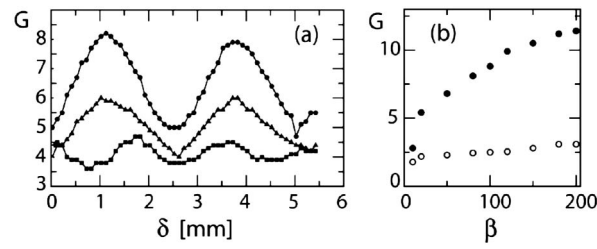
The previous sections have been an overview of recent progress made on the Talbot effect in classical optics and nonlinear optics. One common ground arising from these two categories is that the effect explores only the first-order optical coherence. By exploring high-order optical coherence, the first (to our knowledge) theoretical proposal on the Talbot effect in quantum optics [85] was made with entangled photon pairs and considered in the framework of quantum ghost imaging in 2009. In this work, the authors also considered the self-imaging effect in the framework of quantum lithography, where they found that the Talbot length becomes twice the conventional value [86]. The work immediately attracted considerable attention and triggered further efforts on the phenomenon by considering second-order correlation function and even higher order correlation functions. Ooi and Lan [87] theoretically studied the spatial

Figure 23



Experimental setup for Talbot-effect-enhanced TWM. Reproduced with permission, © 2006. Optical Society of America [83].

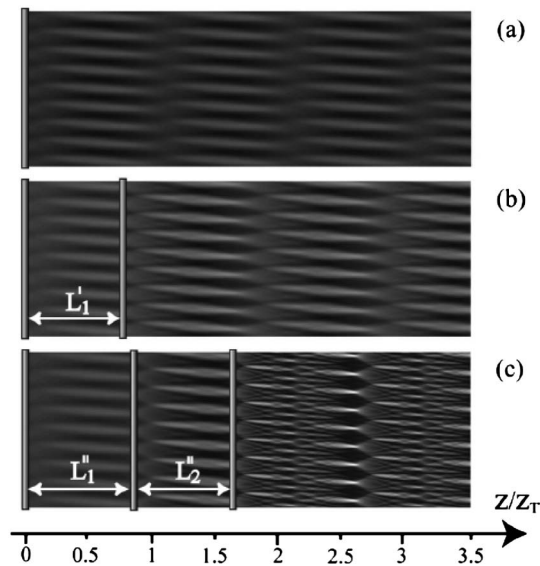
Figure 24



(a) Measured TWM gain as a function of  $\delta$ .  $\delta$  is defined by  $\delta = D - 25.9$  mm, where  $D$  is the distance between the two valves. (b) Gain for one valve (open circles) and two valves (dots).  $\beta$  is the intensity ratio between the pump and signal beams. Reproduced with permission, © 2006. Optical Society of America [83].

interference pattern of the two-photon correlation function for a coherently phased linear array of  $N$  emitters with a double-Raman scheme, each producing nonclassically correlated photon pairs, and showed that the  $N^2$  dependence in the two-photon correlation serves as a coherent amplification method for producing intense nonclassical light. The spatial distribution of the correlation can be controlled by lasers and depends on the detection configuration. Torres-Company with his colleagues [88] theoretically analyzed the self-imaging Talbot effect of entangled photon pairs in the time domain and found rich phenomena appearing in coherence propagation along dispersive media of mode-locked two-photon states with frequency entanglement exhibiting a comblike correlation function. Poem and Silberberg [89] considered the propagation of classical and nonclassical light in multimode optical waveguides and focused on the evolution of the few-photon correlation functions, which, much as the light-intensity distribution in such systems, evolve in a periodic manner,

Figure 25



Simulated Talbot carpets for (a)  $N = 1$ , (b)  $N = 2$ , and (c)  $N = 3$ . Reproduced with permission, © 2006. Optical Society of America [83].

culminating in the “revival” of the initial correlation pattern at the end of each period. They found that, when the input state possesses nontrivial symmetries, the correlation revival period can be longer than that of the intensity, and thus the same intensity pattern can display different correlation patterns. Wu’s and Wang’s groups further performed some experiments on the second-order Talbot effect with both pseudo-thermal light [90,91] and entangled photon pairs [92].

A Bose–Einstein condensate (BEC) is a state of matter of a dilute gas of bosons (e.g., atoms or molecules) cooled to temperatures very near absolute zero (0 K or  $-273.15^{\circ}\text{C}$ ). Under such conditions, a large fraction of the bosons occupy the lowest quantum state, at which point quantum effects become apparent on a macroscopic scale. Two methods, on- and off-resonant absorption imaging, are often experimentally chosen to image the condensate cloud. On-resonant absorption imaging is predominant, despite its limited dynamic range and recoil heating. Off-resonant phase-contrast imaging techniques allow nondestructive and quantitative imaging of BECs, but traditional approaches usually require precisely aligned phase plates or interferometers. Recently, Wen and his colleagues [93] proposed another type of lensless imaging scheme, the electromagnetically induced Talbot effect, for imaging ultracold atoms and molecules. The essential idea of this work is to utilize a strong control standing wave to modify the optical response of the medium to the weak probe field, i.e., an electromagnetically induced grating [94]. The induced nonmaterial grating thus leads to self-images of atoms and molecules in the Fresnel diffraction region.

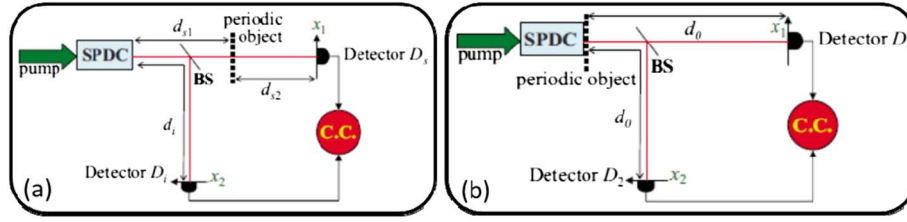
In this section, we review recent progress on the Talbot effect in quantum optics. We pay particular attention to the original proposal of spatial second-order Talbot self-imaging with entangled photon pairs, as well as electromagnetically induced self-imaging.

#### 4.1. Second-Order Talbot Effect in Quantum Imaging

In classical optics, the spatial distribution of a physical object is estimated through the imaging process by measuring the emitted optical radiation or by making use of an optical wave that interacts with the object, via transmission or reflection. The development of ghost imaging (GI) [95] offers an intriguing optical technique to acquire the object’s transverse transmittance pattern by means of photocurrent correlation measurements. The unique features of GI are that an image of the object is reconstructed by correlating the intensities of two spatially correlated beams. One of the beams illuminates the object and is detected by a bucket detector that has no spatial resolution. The other reference beam undergoes only free-space diffraction before impinging on a scanning pinhole detector or a CCD camera with high spatial resolution. The first GI demonstration [96] explored entangled paired photons generated from spontaneous parametric down conversion (SPDC) together with photon-counting bucket and pinhole detectors more than a decade ago. Subsequent realizations with classical and especially (pseudo-)thermal-light sources triggered ongoing efforts on applying GI to remote sensing applications.

In the theoretical proposal by Luo and her coauthors [85], they first considered the setup shown in Fig. 26(a) to study the Talbot effect in a typical quantum GI configuration. The signal and idler photons of wavelengths  $\lambda_s$  and  $\lambda_i$ , respectively, emitted through SPDC in a nonlinear crystal are separated into two beams. An object with periodic structure is placed in the signal arm, and the

Figure 26



Setup to show the Talbot effect in the configuration of (a) quantum imaging and (b) quantum lithography using SPDC photons. (BS, beam splitter; CC, coincidence counter). Figure 1 reprinted with permission from K.-H. Luo *et al.*, Phys. Rev. A 043820 (2009) [85]. Copyright 2009, the American Physical Society. <http://pra.aps.org/abstract/PRA/v80/i4/e043820>

transmitted light is collected by bucket detector  $D_s$ . In the idler arm the detector  $D_i$ , sometimes called the reference detector, is a CCD camera or a scanning point detector, and coincidence measurements are taken. The distance from the output surface of the crystal to the object is  $d_{s1}$  and to the idler detector  $d_i$ ; the distance between the object and detector  $D_s$  is  $d_{s2}$ . To simplify the discussion, the degree of freedom of the light polarization will be ignored.

To show the Talbot effect in the GI configuration, we start with a brief overview of the formulation of GI with SPDC photons. From first-order perturbation theory, the biphoton state at the output surface of the crystal takes the form [95]

$$|\psi\rangle = \int d\omega_s \int d\omega_i \int d^2\alpha_1 \int d^2\alpha_2 \Phi(\omega_s, \omega_i) \delta(\omega_s + \omega_i - \omega_p) \times \delta(\vec{\alpha}_1 + \vec{\alpha}_2) |1_{\vec{k}_s}, 1_{\vec{k}_i}\rangle, \quad (24)$$

where  $\Phi(\omega_s, \omega_i)$  is the spectral function resulting from the phase matching, and  $\omega_s, \omega_i, \vec{k}_s$ , and  $\vec{k}_i$  are the frequencies and wave vectors of the entangled signal and idler waves, respectively. The input pump field is a cw laser at frequency  $\omega_p$ . The detailed form of  $\Phi$  is not important here for transverse correlation of the photons. The  $\delta$  functions imply that the source produces a two-photon state with perfect phase matching. The state of Eq. (24) assumes that the paraxial approximation holds and the factors describing the temporal and transverse behavior of the waves are separable. The frequency correlation determines the two-photon temporal properties while the transverse momentum correlation determines the spatial properties of the pairs. It is the latter wave-vector correlation that is of prime interest in second-order Talbot imaging.

The SPDC signal and idler fields at the detectors are computed in terms of the photon annihilation operators at the output surface of the crystal:

$$E_j^{(+)}(\vec{\rho}_j, z_j, t_j) = \int d\omega_j \int d^2\alpha_j E_j f_j(\omega_j) e^{-i\omega_j t_j} g_j(\vec{\alpha}_j, \omega_j; \vec{\rho}_j, z_j) a(\vec{\alpha}_j, \omega_j), \quad (25)$$

where  $E_j = \sqrt{\hbar\omega_j/2\epsilon_0}$ ,  $\vec{\alpha}_j$  is the transverse wave vector,  $f_j(\omega_j)$  is a narrow bandwidth filter function peaked at central frequency  $\Omega_j$ , and the Green's function  $g_j(\vec{\alpha}_j, \omega_j; \vec{\rho}_j, z_j)$  is the optical transfer function that describes the propagation of each mode of angular frequency  $\omega_j$  from the source to the transverse point  $\vec{\rho}_j$  in the plane of the  $j$ th detector, which is at a distance  $z_j$  from the output surface of

the crystal. The photon annihilation operator at the output surface of the source satisfies the usual commutation relation

$$[a(\vec{\alpha}, \omega), a^\dagger(\vec{\alpha}', \omega')] = \delta(\vec{\alpha} - \vec{\alpha}')\delta(\omega - \omega'). \quad (26)$$

From Glauber's quantum measurement theory, the two-photon coincidence counting rate for two point photodetectors is given by

$$R_{cc} = \frac{1}{T} \int_0^T dt_1 \int_0^T dt_2 |\Psi(\vec{\rho}_1, z_1, t_1; \vec{\rho}_2, z_2, t_2)|^2, \quad (27)$$

where  $T$  is the coincidence window width, and the two-photon or biphoton amplitude  $\Psi$  is characterized by the matrix element between the vacuum state  $|0\rangle$  and the two-photon state  $|\psi\rangle$ ,

$$\Psi(\vec{\rho}_1, z_1, t_1; \vec{\rho}_2, z_2, t_2) = \langle 0 | E_1^{(+)}(\vec{\rho}_1, z_1, t_1) E_2^{(+)}(\vec{\rho}_2, z_2, t_2) | \psi \rangle. \quad (28)$$

Here,  $E_j^{(+)}(\vec{\rho}_j, z_j, t_j)$  ( $j = 1, 2$ ) is the positive frequency part of the electric field at point  $(\vec{\rho}_j, z_j)$  on the  $j$ th detector evaluated at triggering time  $t_j$ , and given in Eq. (25). Equations (24)–(28) outline the basic formulism for quantum GI.

To analyze the Talbot effect in the GI configuration, one needs to obtain the Green's functions in Eq. (25). In the paraxial approximation with an object described by the aperture function  $A_o(\vec{\rho}_o)$ , the Green's functions for the signal and idler beams are given as follows [55,97,98]:

$$g_1(\vec{\alpha}_1, \omega_s; \vec{\rho}_1, d_s) = -\frac{i\omega_s}{2\pi c d_{s2}} e^{\frac{i\omega_s d_s}{c}} e^{\frac{i\omega_s \rho_1^2}{2c d_{s2}}} e^{-\frac{i c d_{s1} \alpha_1^2}{2\omega_s}} \int d^2 \rho_o A_o(\vec{\rho}_o) e^{\frac{i\omega_s \rho_o^2}{2c d_{s2}}} e^{i\vec{\rho}_o \cdot \left(\vec{\alpha}_1 - \frac{\omega_s \vec{\rho}_1}{c d_{s2}}\right)}, \quad (29)$$

$$g_2(\vec{\alpha}_2, \omega_i; \vec{\rho}_2, d_i) = e^{\frac{i\omega_i d_i}{c}} e^{-\frac{i c d_i \alpha_2^2}{2\omega_i}} e^{i\vec{\alpha}_2 \cdot \vec{\rho}_2}, \quad (30)$$

where  $d_s = d_{s1} + d_{s2}$ . With use of Eqs. (24) and (25) under the assumption that  $\omega_j = \Omega_j + \nu_j$  (where  $|\nu_j| \ll \Omega_j$  and  $\Omega_s + \Omega_i = \omega_p$ ), the temporal (or longitudinal) and transverse terms can be factored out so the biphoton amplitude can be represented as

$$\Psi(\vec{\rho}_1, z_1, t_1; \vec{\rho}_2, z_2, t_2) = e^{i(\Omega_s \tau_1 + \Omega_i \tau_2)} \psi(\vec{\rho}_1, \tau_1; \vec{\rho}_2, \tau_2), \quad (31)$$

where  $\tau_1 = t_1 - \frac{d_s}{c}$ ,  $\tau_2 = t_2 - \frac{d_i}{c}$ , and

$$\begin{aligned} & \psi(\vec{\rho}_1, \tau_1; \vec{\rho}_2, \tau_2) \\ &= \int d\nu_s \int d\nu_i \delta(\nu_s + \nu_i) e^{i(\nu_s \tau_1 + \nu_i \tau_2)} f_1(\Omega_s + \nu_s) f_2(\Omega_i + \nu_i) W(\vec{\rho}_1, \vec{\rho}_2). \end{aligned} \quad (32)$$

The transverse part  $W(\vec{\rho}_1, \vec{\rho}_2)$  in Eq. (32) takes the form

$$W(\vec{\rho}_1, \vec{\rho}_2) = W_0 \int d^2 \rho_o A_o(\vec{\rho}_o) e^{\frac{i\omega_s \rho_o^2}{2c d_{s2}}} e^{-i \frac{\omega_s \vec{\rho}_o \cdot \vec{\rho}_1}{c d_{s2}}} \int d^2 \alpha_1 e^{-\frac{i c \alpha_1^2}{2} \left( \frac{d_{s1}}{\omega_s} + \frac{d_i}{\omega_i} \right)} e^{i\vec{\alpha}_1 \cdot (\vec{\rho}_o - \vec{\rho}_2)}, \quad (33)$$

where all the slowly varying terms have been grouped into the constant  $W_0$ .

Completing the integration over the transverse mode  $\vec{\alpha}_1$  in Eq. (33) gives

$$W(\vec{\rho}_1, \vec{\rho}_2) = W_0 \int d^2 \rho_o A_o(\vec{\rho}_o) e^{-\frac{i\omega_s}{c} \vec{\rho}_o \cdot \left( \frac{\vec{\rho}_1}{d_{s2}} + \frac{\vec{\rho}_2}{d_{s1} + \omega_s d / \omega_i} \right)} e^{\frac{i\omega_s}{2c} \vec{\rho}_o^2 \left( \frac{1}{d_{s2}} + \frac{1}{d_{s1} + \omega_s d / \omega_i} \right)}. \quad (34)$$

Here again, all the irrelevant constants have been absorbed into  $W_0$ .

Equation (34) is the starting point to look at the Talbot effect in the configuration of quantum imaging. To catch the essence of the effect, we restrict ourselves to 1D objects, but the extension of the analysis to 2D objects is straightforward. Recall that the aperture function for a general 1D periodic object with the spatial period  $a$  can be expanded as a Fourier series

$$A(x_o) = \sum_{n=-\infty}^{\infty} c_n e^{-\frac{2i\pi n x}{a}}. \quad (35)$$

By plugging Eq. (35) into Eq. (34) and working in the Cartesian coordinate, Eq. (34) now becomes

$$W(x_1, x_2) = W_0 \sum_{n=-\infty}^{\infty} c_n \exp \left( -i \frac{\frac{n^2 \pi}{a^2} \lambda_s}{\frac{1}{d_{s2}} + \frac{1}{d_{s1} + \frac{\lambda_i}{\lambda_s} d_i}} \right) \exp \left( i \frac{\frac{2n\pi}{a} \left( \frac{x_1}{d_{s2}} + \frac{x_2}{d_{s1} + \frac{\lambda_i}{\lambda_s} d_i} \right)}{\frac{1}{d_{s2}} + \frac{1}{d_{s1} + \frac{\lambda_i}{\lambda_s} d_i}} \right). \quad (36)$$

The first exponential term in Eq. (36) is of basic importance to self-imaging and is the “localization” term, since it describes the phase changes of the diffraction orders along the directions of propagation. Self-imaging occurs in planes where the transmitted object light amplitudes are repeated, that is, when all diffraction orders are in phase and interference constructively. From Eq. (36) we see that this can happen at certain distances as the first term equals 1 for all  $n$ ; that is,

$$\frac{1}{d_{s2}} + \frac{1}{d_{s1} + \frac{\lambda_i}{\lambda_s} d_i} = \frac{1}{2ma^2/\lambda_s} = \frac{1}{mz_{sT}}, \quad (37)$$

where  $m$  is an integer and  $z_{sT} = 2a^2/\lambda_s$ . Comparing this with the well-known Gaussian thin lens equation, we can consider the self-imaging to be a counterpart phenomenon in which a sequence of lenses of focal length  $z_{sT}$  is situated in the plane of the periodic object and produces images of the source. The distance  $z_{sT}$  may be regarded as the primary Talbot length for second-order correlation quantum imaging. The factor 2 in Eq. (37) is inconsequential and may be omitted. Thus in the cases where  $m$  is an odd integer, there will be self-images with a lateral shift of half a period relative to the object, due to the  $\pi$  phase shift of odd-number diffraction orders relative to the zero and even-number orders.

In the self-image planes Eq. (36) reduces to

$$W(x_1, x_2) = W_0 \sum_{n=-\infty}^{\infty} c_n \exp \left( i \frac{2n\pi \left( d_{s1} + \frac{\lambda_i}{\lambda_s} d_i \right) x_1 + d_{s2} x_2}{a \left( d_{s1} + d_{s2} + \frac{\lambda_i}{\lambda_s} d_i \right)} \right), \quad (38)$$

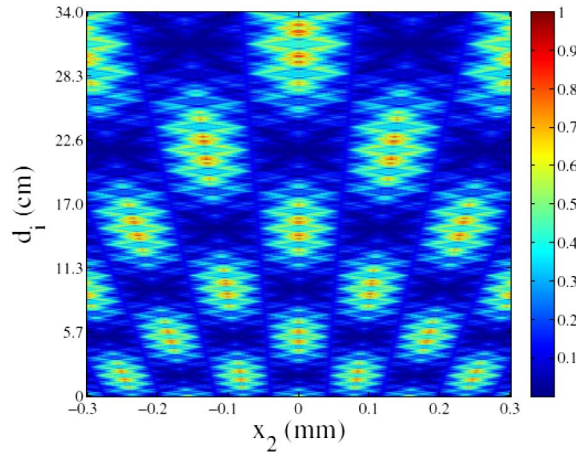
which carries information about the lateral magnification  $M$  of the imaging patterns arising as a result of the nonlocal correlation between entangled photons.



Careful examination of Eq. (38) results in many complex cases with different possible magnifications. Nonetheless, there are two simple cases in which either one of the detectors is fixed at its origin. This corresponds to either  $x_1 = 0$  or  $x_2 = 0$  in Eq. (38), in which case the images are magnified by a factor of  $1 + (d_{s1} + \frac{\lambda_i}{\lambda_s} d_i)/d_{s2}$  or  $1 + d_{s2}/(d_{s1} + \frac{\lambda_i}{\lambda_s} d_i)$ , respectively. It is easy to show that there is no diffraction image if only one detector is used. Figure 27 shows the numerically computed second-order correlation pattern obtained by scanning the idler detector  $D_i$  along the longitudinal  $z$  and transverse  $x$  directions while keeping the signal detector ( $D_s$ ) fixed at position  $d_{s2}$  and  $x_1 = 0$ , the distance  $d_{s1}$  from the crystal to the periodic object also being fixed. We see that a typical Talbot carpet pattern is created. In the simulation, it was assumed that both idler and signal photons were generated by SPDC at the wavelength  $\lambda_s = \lambda_i = \lambda = 883.2$  nm when light from a 441.6 nm pump laser beam was incident on a nonlinear crystal, and the periodic object was a 1D rectangular grating with  $a = 0.1$  nm.

The theoretical predictions of Eqs. (37) and (38) were experimentally confirmed by Wang's group in 2010 [92]. Their experimental setup is shown at the top of Fig. 28, where a 5 mm  $\times$  5 mm  $\times$  3 mm beta-barium-borate (BBO) crystal was cut for Type I phase matching. The crystal was pumped by the second harmonic of a Ti:sapphire femtosecond laser with center wavelength at 400 nm, beam diameter 3 mm, and repetition rate 76 MHz. The downconverted signal and idler photons were spectrally filtered by an interference filter of 10 nm bandwidth centered at 800 nm. The time window of 4 ns was chosen for coincidence counts. The imaged grating was fabricated with period 400  $\mu$ m and slit width 180  $\mu$ m. These parameters defined the Talbot length as  $z_T = 40$  cm. By fixing Detector 1, scanning Detector 2 in its transverse plane yielded the self-image of the

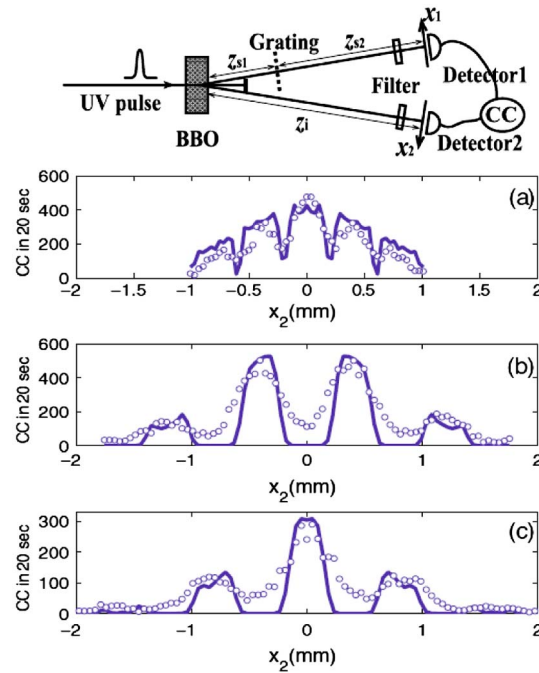
Figure 27



Second-order Talbot imaging carpet obtained by scanning the idler detector  $D_i$  through  $d_i = 0$ –34 cm along the longitudinal  $z$  direction and through  $x_2 = -0.3$ –0.3 mm in the transverse  $x$  direction while fixing the signal detector  $D_s$  at position  $d_{s2} = 20$  cm and  $x_1 = 0$ , and  $d_{s1} = 11$  cm. The color bar denotes the transverse value of the two-photon correlation function. Figure 2 reprinted with permission from K.-H. Luo *et al.*, Phys. Rev. A 043820 (2009) [85]. Copyright 2009, the American Physical Society. <http://pra.aps.org/abstract/PRA/v80/i4/e043820>



Figure 28



Top: Experimental setup for two-photon second-order Talbot self-imaging in the ghost interference scheme. The open circles in (a)–(c) are the coincidence counts for three different diffraction lengths of (a)  $z_T/4$  ( $z_i = 12$  cm,  $z_{s1} = 8$  cm,  $z_{s2} = 20$  cm), (b)  $z_T/2$  ( $z_i = 25$  cm,  $z_{s1} = 15$  cm,  $z_{s2} = 40$  cm), and (c)  $z_T$  ( $z_i = 25$  cm,  $z_{s1} = 55$  cm,  $z_{s2} = 80$  cm). The solid lines are theoretical curves. Figure 2 reprinted with permission from X.-B. Song *et al.*, Phys. Rev. Lett. 033902 (2011) [92]. Copyright 2011, the American Physical Society. <http://prl.aps.org/abstract/PRL/v107/i3/e033902>

grating in the two-photon joint detections. In such a case, the periodic structure can be enlarged by a magnification of  $1 + (z_{s1} + z_i)/z_{s2}$ . If one imagines Detector 2 to be a source that emits a ray to the grating after reflection off the crystal, the present scheme is comparable with the previous one. The experimental results given in Figs. 28(a)–28(c) were made for three different diffraction lengths. It is readily seen that, in all three cases, the magnification is 2, while the image period is  $400\text{ }\mu\text{m}$  in Fig. 28(a) and  $800\text{ }\mu\text{m}$  in Figs. 28(b) and 28(c). The experimental data (open circles) basically agree with the theoretical curves (solid lines), thus verifying the correctness of the above theoretical analysis on the second-order Talbot effect with entangled light. In the experiment, the coincidence counts were a few hundred in 20 s. The single counts in either the signal detector or the idler detector were about 10 times higher than the coincidences within the same detecting time window.

The extension of the second-order Talbot effect with incoherent light was soon performed independently and simultaneously by Wu's group [90] and Wang's group [91]. By replacing the entangled photon source with pseudo-thermal light, the two groups experimentally demonstrated the Talbot self-imaging in a thermal GI setup. These studies further confirm the common belief in the GI community that thermal light can be used to mimic certain features of quantum light sources. Indeed, besides the low-visibility, second-order Talbot

self-imaging with thermal light reveals most features observed with SPDC photon pairs.

## 4.2. Second-Order Talbot Effect in Quantum Lithography

In the proof-of-principle quantum lithography experiment [99], the spatial resolution improvement by a factor of 2 over classical optics was achieved by letting downconverted SPDC photons simultaneously pass through the same slit. This prompts a question about whether there is any difference in the Talbot self-imaging effect; see Fig. 26(b). Such a question was answered theoretically in [85,86] and experimentally in [92]. They found that for the Talbot effect, there is no gain in spatial resolution but the Talbot length is enlarged twice. This can be shown as follows. As shown in Fig. 26(b), the periodic object was placed right behind the SPDC source, and the source produced degenerate signal and idler photon pairs. The distance between the object and the detectors was  $d_0$ . The Green's function for both signal ( $j = 1$ ) and idler ( $j = 2$ ) photons now has the form of

$$g_j(\vec{\alpha}_j, \omega; \vec{\rho}_j, d) = -\frac{i}{\lambda d} e^{\frac{i\omega d}{c}} e^{\frac{i\omega \rho_j^2}{2cd}} \int d^2 \rho_o A_o(\vec{\rho}_o) e^{\frac{i\omega \rho_o^2}{2cd}} e^{i\vec{\rho}_o \cdot (\vec{\alpha}_j - \frac{\omega \vec{\rho}_j}{cd})}. \quad (39)$$

The transverse part of the two-photon amplitude (32) then becomes

$$W(\vec{\rho}_1, \vec{\rho}_2) = W_0 \int d^2 \rho_o A_o^2(\vec{\rho}_o) e^{\frac{i\omega \rho_o^2}{cd}} e^{-\frac{i\omega}{cd} \vec{\rho}_o \cdot (\vec{\rho}_1 + \vec{\rho}_2)}. \quad (40)$$

Substituting Eq. (35) into Eq. (40) gives

$$W(x_1, x_2) = W_0 \sum_{n=-\infty}^{\infty} c'_n e^{-\frac{i\pi n^2}{2a^2} d_0} e^{i\frac{\pi n}{a}(x_1 + x_2)}, \quad (41)$$

with the new coefficient  $c'_n = \sum_{l=-\infty}^{\infty} c_l c_{n-l}$ . Thus, the condition for revival patterns of the periodic structure to occur (in which the diffraction orders have equal phases) is

$$d_0 = m \frac{4a^2}{\lambda} = mz_{sT}, \quad (42)$$

and reduces Eq. (41) to a simple form

$$W(x_1, x_2) = W_0 \sum_{n=-\infty}^{\infty} c'_n e^{i\frac{\pi n}{a}(x_1 + x_2)}. \quad (43)$$

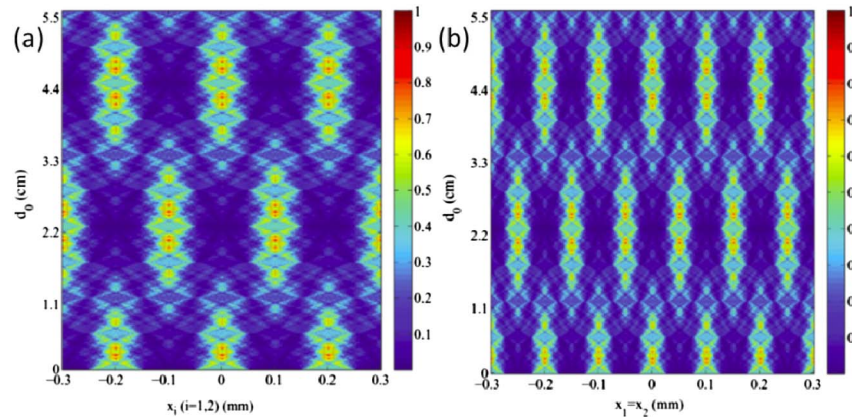
From Eq. (42) we see that, for a source of the same wavelength, the primary second-order Talbot length  $z_{sT} = 4a^2/\lambda$  is twice the classical Talbot length, which coincides with the conclusions drawn by Ooi and Lan [87] and Song *et al.* [92]. As we can see from Eq. (43), when one of the detectors is fixed and the other scanned, there is a magnification factor of 2. When both detectors are moved synchronously, however, the image period is reduced by a factor of 2. Thus, the two factors cancel each other in the configuration of quantum lithography and lead to no net improvement in the spatial resolution. This is in contrast to the original proposal for quantum lithography [100] and the proof-of-principle

experiment for two-photon diffraction and quantum lithography [97], where the object was nonperiodic.

By applying the same parameters as in Fig. 27, Fig. 29(a) shows the second-order interference pattern obtained by scanning both detectors along the  $z$  direction in the region of  $d_0 = 0$ –5.7 cm while fixing the transverse position of one detector ( $D_s$  or  $D_i$ ) at  $x_1 = 0$  (or  $x_2 = 0$ ) and scanning the other detector in its transverse direction. In such a case, there is a magnification factor of 2, as evidenced in Fig. 29(a). When both detectors are moved synchronously along the transverse direction, the period of the image is halved; that is, the longitudinal resolution is enhanced by a factor of 2. Thus the two factors cancel each other and result in no spatial resolving power enhancement; see Fig. 29(b).

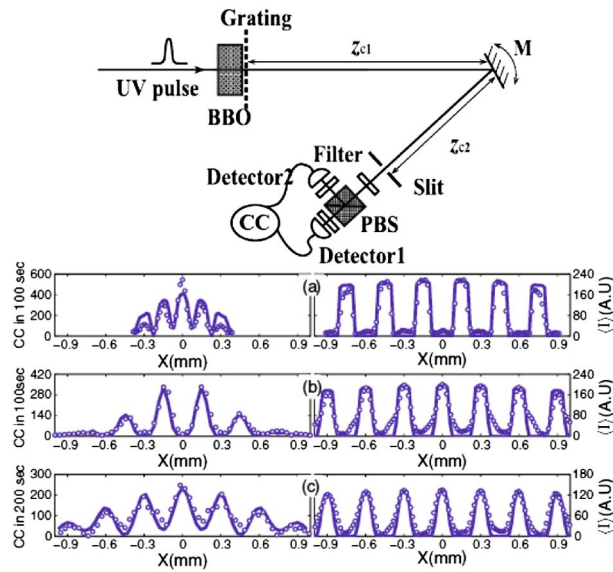
The experiment performed by Song and his colleagues [92] verified the theoretical predictions of Eqs. (42) and (43). Their experimental setup is sketched at the top of Fig. 30. The 400 nm pulsed beam was used to pump a 5 mm × 5 mm × 2 mm Type II BBO crystal to generate collinear orthogonally polarized photon pairs. The grating was placed immediately after the crystal. The slit, polarizing beam splitter, and coincidence circuit work together as a two-photon absorber. For convenience, instead of moving the two detectors, in the experiment they rotated the mirror M to “scan” the diffraction pattern across the detector surfaces. The coincidence time window was set to about 2 ns. The grating was chosen with period of 300 μm and slit width of 120 μm, corresponding to a classical Talbot length of  $z_T = 22.5$  cm for light wavelength at  $\lambda = 800$  nm. In three different cases where  $z_{c1} + z_{c2} = (z_{sT}/4, z_{sT}/2, z_{sT})$ , the observed self-imaging patterns are shown in the left parts of Figs. 30(a)–30(c) respectively. The experimental data and theoretical curves are indicated by open circles and solid lines, respectively. To see the difference of the Talbot effect with entangled

Figure 29



Second-order Talbot lithography carpets obtained by (a) scanning both detectors  $D_i$  and  $D_s$  along the  $z$  direction from  $d_0 = 0$  to 5.7 cm with the transverse position of one detector fixed at  $x_1(x_2) = 0$ , and the other detector scanned in its transverse  $x_2(x_1)$  direction; (b) moving both detectors simultaneously in the same manner along the transverse  $x$  and longitudinal  $z$  directions, with transverse scanning range  $x_1 = x_2 = -0.3$  to 0.3 mm. The color bars denote the values of the transverse two-photon correlation functions. Figure 5 reprinted with permission from K.-H. Luo *et al.*, Phys. Rev. A 029902 (2011) [86]. Copyright 2011, the American Physical Society. <http://pra.aps.org/abstract/PRA/v83/i2/e029902>

Figure 30



Top: Experimental setup for observing two-photon second-order Talbot self-imaging in the quantum lithography configuration. The open circles are experimental data observed for three diffraction lengths of (a)  $z_{sT}/4$ , (b)  $z_{sT}/2$ , and (c)  $z_{sT}$ . The left and right parts correspond to the entangled two-photon source and the coherent light source, respectively. The solid lines are theoretical curves. Figure 3 reprinted with permission from X.-B. Song *et al.*, Phys. Rev. Lett. 033902 (2011) [92]. Copyright 2011, the American Physical Society. <http://prl.aps.org/abstract/PRL/v107/i3/e033902>

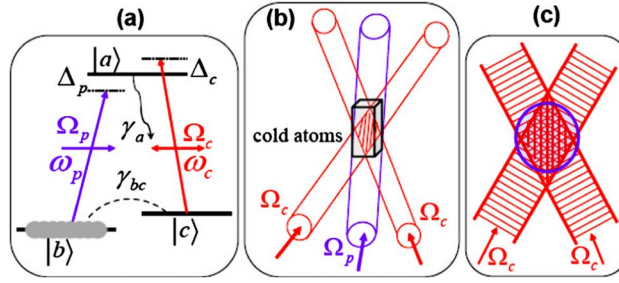
photons from coherent sources, the authors further experimentally checked the self-imaging with coherent light sources under the same conditions. The right parts of Figs. 30(a)–30(c) show the recorded self-images with coherent light. By comparing the left parts with the right in Figs. 30(a)–30(c), it becomes clear now that the image resolution is indeed not improved by a factor of 2, but the Talbot length is doubled.

### 4.3. Electromagnetically Induced Talbot Effect

Optical imaging offers a powerful diagnostic methodology for a variety of experiments involving ultracold atoms and molecules, i.e., BECs. Besides the on-/off-resonant absorption imaging, other imaging techniques, such as dark-ground imaging, *in situ* imaging, and time-of-flight imaging, have also been proposed and demonstrated to form BEC images.

In 2011 a new imaging technique, namely, the electromagnetically induced Talbot effect [93], was theoretically proposed for imaging ultracold atoms and molecules. Figure 31 illustrates a medium of length  $L$  consisting of an ensemble of closed three-level atoms (or molecules) in the  $\Lambda$  configuration, with two metastable lower states. Two ground states  $|b\rangle$  and  $|c\rangle$  are coupled to the excited state  $|a\rangle$  via a strong control field of angular frequency  $\omega_c$  near resonance on the  $|c\rangle \rightarrow |a\rangle$  transition with a detuning  $\Delta_c = \omega_c - \omega_{ac}$ , and a weak probe field of angular frequency  $\omega_p$  close to resonance on the  $|b\rangle \rightarrow |a\rangle$  transition with a detuning  $\Delta_p = \omega_p - \omega_{ab}$ . The control light consists of two strong fields

Figure 31



(a) Closed three-level  $\Lambda$ -type atomic system for electromagnetically induced self-imaging. (b) Configuration of forming an electromagnetically induced grating (EIG). (c) Snapshot of the EIG in (b). Reprinted with permission from Wen *et al.*, Appl. Phys. Lett. **98**, 081108 (2011) [93]. Copyright 2011, American Institute of Physics.

that are symmetrically displaced with respect to  $z$  and whose intersection generates a standing wave within the medium; see Fig. 31(b) and the snapshot Fig. 31(c). The two cw control fields share the same Rabi frequency  $\Omega_c$ , and all the population is initially distributed in the ground state  $|b\rangle$ .

By solving the atomic dynamics, the linear susceptibility of the system at the probe frequency is

$$\chi = \frac{N|\mu|^2}{2\hbar\epsilon_0} \frac{\Delta_2 + i\gamma_{bc}}{|\Omega_c|^2 \cos^2\left(\frac{\pi x}{a}\right) - (\Delta_p + i\gamma_a)(\Delta_2 + i\gamma_{bc})}, \quad (44)$$

where  $N$  is the atomic density,  $\Delta_2 = \Delta_p - \Delta_c$  is the two-photon detuning,  $a$  is the spatial period of the standing wave along the  $x$  direction perpendicular to the propagation direction  $z$ , and  $\gamma_a$  and  $\gamma_{bc}$  are the decay rate of  $|a\rangle$  and dephasing rate between  $|b\rangle$  and  $|c\rangle$ , respectively. Here  $a$  can be made arbitrarily larger than the wavelength  $\lambda_p$  of the probe field by varying the angle between the two wave vectors of two control beams. The propagation dynamics of the probe field within the cloud obeys the Maxwell's equation and its transmitted amplitude at the output surface is

$$E_p(x, L) = E_p(x, 0) e^{-\frac{k_p \chi'' L}{2}} e^{i \frac{k_p \chi' L}{2}}, \quad (45)$$

where the linear susceptibility expressed in Eq. (40) is decomposed into its real and imaginary parts  $\chi = \chi' + i\chi''$ , and  $E_p(x, 0)$  is the input probe-field profile. Because of the periodicity exhibited in Eq. (44), the output field in Eq. (45) may be recast into Fourier series. That is,

$$E_p(x, L) = \sum_{n=-\infty}^{\infty} c_n e^{i \frac{2\pi n x}{a}}. \quad (46)$$

With the substitution of Eq. (46) into Eq. (3), it is not difficult to show that the diffracted field at a distance  $z_T$  from the output surface of the medium can repeat itself. Alternatively, the conventional Talbot effect is recovered in the current

atomic system. The *in situ* images of degenerate clouds of BEC can be obtained by analyzing the intensity patterns of the output probe field, in particular, their peak and valley intensities. In comparison with the on-/off-resonant absorption imaging techniques, the current scheme does not destroy the condensate atoms since it only heats the condensate atoms with a small percentage by adjusting the probe detuning. We remark here that the scheme is only in its theoretical infancy. Further theoretical and experimental investigations are necessary to turn the idea into practice.

The effect described here is capable of lensless imaging and may reduce the influence from vibrations in the experiment. Thus, it could be useful for imaging BEC on a chip and an optical lattice. In practice, the imaging quality may be affected by the finite dimensions of the standing wave and the size of the input probe field. For visible light, the Talbot length here is estimated to be several tens of millimeters. To simplify the observation, a secondary imaging process would thus be necessary to magnify the self-images as implemented in [79]. Moreover, by manipulating the input fields, the induced Talbot effect may find applications in nonlinear parametric conversions, in which the modulated optical responses could enhance the nonlinearities under some conditions. It would also be interesting to apply this technique to investigate the dynamics of the formation, decay, and collapse of the condensates.

## 5. Summary

The Talbot self-imaging phenomenon has captured the attention and interest of people from a variety of research areas since its first demonstration with white light nearly 180 years ago. Its simplicity and beauty have undoubtedly created extensive theoretical and experimental studies. After centuries of effort, it seems to us at this moment that the principles of optical systems using one or more periodic structures performing under various coherence conditions of illuminating radiation are fairly well understood. The extension of the phenomenon to other research fields, such as cold atoms/molecules, waveguides, and x ray not only enriches the scope of theoretical analysis but also opens doors for a variety of potential applications. Despite the rapid progress made in recent years, it is believed that many significant works are yet to appear. The interdisciplinary research will lead to discoveries within the broad class of self-imaging. From this point of view, our paper is just a starting point for future research on the phenomenon. We will not be surprised as new observations on self-imaging continue to appear.

## Acknowledgments

This work is supported by the National Basic Research Program of China (contract 2012CB921804), the National Natural Science Foundation of China (NSFC, grants 11004097, 61222503, and 11274162), the Fundamental Research Funds for the Central Universities (contracts 1095021339 and 1124021319), the New Century Excellent Talents in University, and the Priority Academic Program Development of Jiangsu Higher Education Institutions (PAPD).



## References

1. H. F. Talbot, "Facts relating to optical science," *Philos. Mag.* **9**, 401–407 (1836).
2. Lord Rayleigh, "On copying diffraction gratings and on some phenomenon connected therewith," *Philos. Mag.* **11**, 196–205 (1881).
3. A. Winkelmann, "Übereinige Erscheinungen, die bei der Beugung des Lichtes durch Gitter Auftreten," *Ann. Phys. (Leipzig)* **332**, 905–954 (1908).
4. H. Weisel, "Über die nach Fresnelscher Art Beobachteten Beugungsercheinungen der Gitter," *Ann. Phys. (Leipzig)* **338**, 995–1031 (1910).
5. M. Wolfke, "Über die Abbildung eines Gitters Au erhaldd der Einstellenebene," *Ann. Phys. (Leipzig)* **345**, 194–200 (1913).
6. J. M. Cowley and A. F. Moodie, "Fourier images I. The point source," *Proc. Phys. Soc. (London) B* **70**, 486–496 (1957).
7. J. M. Cowley and A. F. Moodie, "Fourier images II. The out-of-focus patterns," *Proc. Phys. Soc. (London) B* **70**, 497–504 (1957).
8. J. M. Cowley and A. F. Moodie, "Fourier images III. Finite sources," *Proc. Phys. Soc. (London) B* **70**, 505–513 (1957).
9. J. M. Cowley and A. F. Moodie, "Fourier images IV. The phase grating," *Proc. Phys. Soc. London* **76**, 378–384 (1960).
10. G. L. Rogers, "Interesting paradox in Fourier images," *J. Opt. Soc. Am.* **62**, 917–918 (1972).
11. J. T. Winthrop and C. R. Worthington, "Theory of Fresnel images. I. Plane periodic objects in monochromatic light," *J. Opt. Soc. Am.* **55**, 373–381 (1965).
12. W. D. Montgomery, "Self-imaging objects of infinite aperture," *J. Opt. Soc. Am.* **57**, 772–778 (1967).
13. K. Paturski, "The self-imaging phenomenon and its applications," in *Progress in Optics*, E. Wolf, ed. (North-Holland, 1989), Vol. **27**, pp. 1–108.
14. J. M. Cowley, *Diffraction Physics* (North-Holland, 1995).
15. M. V. Berry, I. Marzoli, and W. P. Schleich, "Quantum carpets, carpets of light," *Phys. World* **14**(6), 39–44 (2001).
16. D. Wojcik, I. Bialynicki-Birula, and K. Zyczkowski, "Time evolution of quantum fractals," *Phys. Rev. Lett.* **85**, 5022–5025 (2000).
17. C. Leichtle, I. S. Averbukh, and W. P. Schleich, "Generic structures of multilevel quantum beats," *Phys. Rev. Lett.* **77**, 3999–4002 (1996).
18. M. V. Berry and S. Klein, "Integer, fractional and fractal Talbot effects," *J. Mod. Opt.* **43**, 2139–2164 (1996).
19. H. Mack, M. Bienert, F. Haug, M. Freyberger, and W. P. Schleich, "Wave packets can factorize numbers," *Phys. Status Solidi B* **233**, 408–415 (2002).
20. R. W. Robinett, "Quantum wave packet revivals," *Phys. Rep.* **392**, 1–119 (2004).
21. E. Lau, "Beugungsercheinungen an Doppelrastern," *Ann. Phys. (Leipzig)* **6**, 417–423 (1948).
22. M. S. Chapman, C. R. Ekstrom, T. D. Hammond, R. A. Rubenstein, J. Schmiedmayer, S. Wehinger, and D. E. Pritchard, "Optics and interferometer with Na molecules," *Phys. Rev. Lett.* **74**, 4783–4786 (1995).
23. L. Deng, E. W. Hagley, J. Denschlag, J. E. Simsarian, M. Edwards, C. W. Clark, K. Helmerson, S. L. Rolston, and W. D. Phillips, "Temporal, matter-wave-dispersion Talbot effect," *Phys. Rev. Lett.* **83**, 5407–5411 (1999).

24. B. Brezger, L. Hackermuller, S. Uttenthaler, J. Petschinka, M. Arndt, and A. Zeilinger, "Matter-wave interferometer for large molecules," *Phys. Rev. Lett.* **88**, 100404 (2002).
25. K. Hornberger, S. Gerlich, P. Haslinger, S. Nimmrichter, and M. Arndt, "Colloquium: quantum interference of clusters and molecules," *Rev. Mod. Phys.* **84**, 157–173 (2012).
26. T. Jansson and J. Jansson, "Temporal self-imaging effect in single-mode fibers," *J. Opt. Soc. Am.* **71**, 1373–1376 (1981).
27. F. Mitschke and U. Morgner, "The temporal Talbot effect," *Opt. Photon. News* **9**(6), 45–47 (1998).
28. J. Azana and M. A. Muriel, "Temporal Talbot effect in fiber gratings and its applications," *Appl. Opt.* **38**, 6700–6704 (1999).
29. J. Azana and M. A. Muriel, "Technique for multiplying the repetition rates of periodic trains of pulses by means of a temporal self-imaging effect in chirped fiber gratings," *Opt. Lett.* **24**, 1672–1674 (1999).
30. J. Azana and M. A. Muriel, "Temporal self-imaging effects: theory and application for multiplying pulse repetition rates," *IEEE J. Quantum Electron.* **7**, 728–744 (2001).
31. J. Azana, "Spectral Talbot phenomena of frequency combs induced by cross-phase modulation in optical fibers," *Opt. Lett.* **30**, 227–229 (2005).
32. J. A. Bolger, P. Hu, J. T. Mok, J. L. Blows, and B. J. Eggleton, "Talbot self-imaging and cross-phase modulation for generation of tunable high repetition rate pulse trains," *Opt. Commun.* **249**, 431–439 (2005).
33. J. P. Guigay, "On Fresnel diffraction by one-dimensional periodic objects, with application to structure determination of phase objects," *Opt. Acta* **18**, 677–682 (1971).
34. J. Westerholm, J. Turunen, and J. Huttunen, "Fresnel diffraction in fractional Talbot planes: a new formulation," *J. Opt. Soc. Am. A* **11**, 1283–1290 (1994).
35. H. Hamam, "Simplified linear formulation of Fresnel diffraction," *Opt. Commun.* **144**, 89–98 (1997).
36. V. Arrizon and J. Ojeda-Castaneda, "Fresnel diffraction of substructured gratings: matrix description," *Opt. Lett.* **20**, 118–120 (1995).
37. V. Arrizon, J. G. Ibarra, and J. Ojeda-Castaneda, "Matrix formulation of the Fresnel transform of complex transmittance gratings," *J. Opt. Soc. Am. A* **13**, 2414–2422 (1996).
38. S. B. Tucker, J. Ojeda-Castaneda, and W. T. Cathey, "Matrix description of near-field diffraction and the fractional Fourier transform," *J. Opt. Soc. Am. A* **16**, 316–322 (1999).
39. C.-S. Guo, X. Yin, L.-W. Zhu, and Z.-P. Hong, "Analytical expression for phase distribution of a hexagonal array at fractional Talbot planes," *Opt. Lett.* **32**, 2079–2081 (2007).
40. L.-W. Zhu, X. Yin, Z.-P. Hong, and C.-S. Guo, "Reciprocal vector theory for diffractive self-imaging," *J. Opt. Soc. Am. A* **25**, 203–210 (2008).
41. A. W. Lohmann and J. A. Thomas, "Making an array illuminator based on the Talbot effect," *Appl. Opt.* **29**, 4337–4340 (1990).
42. T. J. Suleski, "Generation of Lohmann images from binary-phase Talbot array illuminators," *Appl. Opt.* **36**, 4686–4691 (1997).
43. P. Xi, C. Zhou, E. Dai, and L. Liu, "Generation of near-field hexagonal array illumination with a phase grating," *Opt. Lett.* **27**, 228–230 (2002).

44. M. Testorf, "Designing Talbot array illuminators with phase-space optics," *J. Opt. Soc. Am. A* **23**, 187–192 (2006).
45. J. Ojeda-Castaneda and E. E. Sicre, "Quasi ray-optical approach to longitudinal periodicities of free and bounded wavefields," *Opt. Acta* **32**, 17–26 (1985).
46. M. Testorf and J. Ojeda-Castaneda, "Fractional Talbot effect: analysis in phase space," *J. Opt. Soc. Am. A* **13**, 119–125 (1996).
47. M. Testorf, B. Hennelly, and J. Ojeda-Castaneda, *Phase-Space Optics* (McGraw Hill, 2010).
48. R. Ulrich, "Image formation by phase coincidences in optical waveguides," *Opt. Commun.* **13**, 259–264 (1975).
49. L. B. Soldano and E. C. M. Pennings, "Optical multi-mode interference devices based on self-imaging: Principles and applications," *J. Lightwave Technol.* **13**, 615–627 (1995).
50. R. Iwanow, D. A. May-Arrioja, D. N. Christodoulides, G. I. Stegeman, Y. Min, and W. Sohler, "Discrete Talbot effect in waveguide arrays," *Phys. Rev. Lett.* **95**, 053902 (2005).
51. V. Raghunathan, H. Renner, R. R. Rice, and B. Jalali, "Self-imaging silicon Raman amplifier," *Opt. Express* **15**, 3396–3405 (2007).
52. Y. Wang, K. Zhou, X. Zhang, K. Yang, Y. Wang, Y. Song, and S. Liu, "Discrete plasmonic Talbot effect in subwavelength metal waveguide arrays," *Opt. Lett.* **35**, 685–687 (2010).
53. A. W. Lohmann and J. Ojeda-Castaneda, "Spatial periodicities in partially coherent fields," *Opt. Acta* **30**, 475–479 (1983).
54. G. Indebetouw, "Propagation of spatially periodic wavefields," *Opt. Acta* **31**, 531–539 (1984).
55. J. W. Goodman, *Introduction to Fourier Optics* (McGraw-Hill, 1968).
56. J. R. Leger, "Lateral mode control of an AlGaAs laser array in a Talbot cavity," *Appl. Phys. Lett.* **55**, 334–336 (1989).
57. D. Mehuys, W. Streifer, R. G. Waats, and D. F. Welch, "Modal analysis of linear Talbot-cavity semiconductor lasers," *Opt. Lett.* **16**, 823–825 (1991).
58. C. J. Corcoran and F. Durville, "Experimental demonstration of a phase-locked laser array using a self-Fourier cavity," *Appl. Phys. Lett.* **86**, 201118 (2005).
59. M. R. Dennis, N. I. Zheludev, and F. Javier Garcia de Abajo, "The plasmon Talbot effect," *Opt. Express* **15**, 9692–9700 (2007).
60. A. Maradudin and T. Leskova, "The Talbot effect for a surface plasmon polariton," *New J. Phys.* **11**, 033004 (2009).
61. G. Niconoff, J. Sanchez-Gil, H. Sanchez, and A. Leija, "Self-imaging and caustics in two-dimensional surface plasmon optics," *Opt. Commun.* **281**, 2316–2320 (2008).
62. W. Zhang, C. Zhao, J. Wang, and J. Zhang, "An experimental study of the plasmonic Talbot effect," *Opt. Express* **17**, 19757–19762 (2009).
63. S. Cherukulappurath, D. Heinis, J. Cesario, N. F. van Hulst, S. Enoch, and R. Quidant, "Local observation of plasmon focusing in Talbot carpets," *Opt. Express* **17**, 23772–23784 (2009).
64. W. Zhang, X. Huang, and Z. Lu, "Super Talbot effect in indefinite meta-material," *Opt. Express* **19**, 15297–15303 (2011).
65. O. Bryngdahl, "Image formation using self-imaging techniques," *J. Opt. Soc. Am.* **63**, 416–419 (1973).

66. R. Ulrich, "Light-propagation and imaging in planar optical waveguides," *Nouv. Rev. Opt.* **6**, 253–262 (1975).
67. H. Ramezani, D. N. Christodoulides, V. Kovanis, I. Vitebskiy, and T. Kottos, "PT-symmetric Talbot effects," *Phys. Rev. Lett.* **109**, 033902 (2012).
68. P. Cloetens, J. P. Guigay, C. De Martino, J. Baruchel, and M. Schlenker, "Fractional Talbot imaging of phase gratings with hard x rays," *Opt. Lett.* **22**, 1059–1061 (1997).
69. C. David, B. Nohammer, H. H. Solak, and E. Ziegler, "Differential x-ray phase contrast imaging using a shearing interferometer," *Appl. Phys. Lett.* **81**, 3287–3289 (2002).
70. A. Momose, "Demonstration of x-ray Talbot interferometry," *Jpn. J. Appl. Phys.* **42**, L866–L868 (2003).
71. T. Weitkamp, B. Nohammer, A. Diaz, C. David, and E. Ziegler, "X-ray wavefront analysis and optics characterization with a grating interferometer," *Appl. Phys. Lett.* **86**, 054101 (2005).
72. A. Momose, W. Yashiro, Y. Takeda, Y. Suzuki, and T. Hattori, "Phase tomography by x-ray Talbot interferometry for biological imaging," *Jpn. J. Appl. Phys.* **45**, 5254–5262 (2006).
73. T. Weitkamp, A. Diaz, C. David, F. Pfeiffer, M. Stampanoni, P. Cloetens, and E. Ziegler, "X-ray phase imaging with a grating interferometer," *Opt. Express* **13**, 6296–6304 (2005).
74. W. Yashiro, Y. Takeda, and A. Momose, "Efficiency of capturing a phase image using cone-beam x-ray Talbot interferometry," *J. Opt. Soc. Am. A* **25**, 2025–2039 (2008).
75. F. Pfeiffer, T. Weitkamp, O. Bunk, and C. David, "Phase retrieval and differential phase-contrast imaging with low-brilliance x-ray sources," *Nat. Phys.* **2**, 258–261 (2006).
76. F. Pfeiffer, M. Bech, O. Bunk, P. Kraft, E. F. Eikenberry, Ch. Bronnimann, C. Grunzweig, and C. David, "Hard-x-ray dark-field imaging using a grating interferometer," *Nat. Mater.* **7**, 134–137 (2008).
77. P. Peier, S. Pilz, F. Muller, K. A. Nelson, and T. Feurer, "Analysis of phase contrast imaging of terahertz phonon-polaritons," *J. Opt. Soc. Am. B* **25**, B70–B75 (2008).
78. B. J. McMorran and A. D. Cronin, "An electron Talbot interferometer," *New J. Phys.* **11**, 033021 (2009).
79. Y. Zhang, J.-M. Wen, S. N. Zhu, and M. Xiao, "Nonlinear Talbot effect," *Phys. Rev. Lett.* **104**, 183901 (2010).
80. J.-M. Wen, Y. Zhang, S. N. Zhu, and M. Xiao, "Theory of nonlinear Talbot effect," *J. Opt. Soc. Am. B* **28**, 275–280 (2011).
81. Z. Chen, D. Liu, Y. Zhang, J. M. Wen, S. N. Zhu, and M. Xiao, "Fractional second-harmonic Talbot effect," *Opt. Lett.* **37**, 689–691 (2012).
82. D. Liu, Y. Zhang, Z. Chen, J.-M. Wen, and M. Xiao, "Acousto-optic tunable second-harmonic Talbot effect based on periodically poled LiNbO<sub>3</sub> crystals," *J. Opt. Soc. Am. B* **29**, 3325–3329 (2012).
83. U. Bortolozzo, S. Residori, and J. P. Huignard, "Enhancement of the two-wave-mixing gain in a stack of thin nonlinear media by use of the Talbot effect," *Opt. Lett.* **31**, 2166–2168 (2006).
84. M. Paturzo, P. De Natale, S. De Nicol, P. Ferraro, S. Mailis, R. Eason, G. Coppola, M. Iodice, and M. Gioffre, "Tunable two-dimensional hexagonal phase array in domain-engineered Z-cut lithium niobate crystal," *Opt. Lett.* **31**, 3161–3166 (2006).

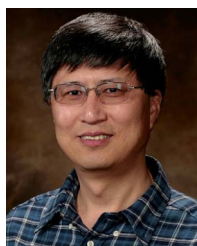
85. K.-H. Luo, J.-M. Wen, X.-H. Chen, Q. Liu, M. Xiao, and L.-A. Wu, "Second-order Talbot effect with entangled photon pairs," *Phys. Rev. A* **80**, 043820 (2009).
86. K.-H. Luo, J.-M. Wen, X.-H. Chen, Q. Liu, M. Xiao, and L.-A. Wu, "Erratum: Second-order Talbot effect with entangled photon pairs," *Phys. Rev. A* **83**, 029902 (2011).
87. C. H. R. Ooi and B. L. Lan, "Intense nonclassical light: controllable two-photon Talbot effect," *Phys. Rev. A* **81**, 063832 (2010).
88. V. Torres-Company, J. Lancis, H. Lajunen, and A. T. Friberg, "Coherence revivals in two-photon frequency combs," *Phys. Rev. A* **84**, 033830 (2011).
89. E. Poem and Y. Silberberg, "Photon correlations in multimode waveguides," *Phys. Rev. A* **84**, 041805(R) (2011).
90. K.-H. Luo, X.-H. Chen, Q. Liu, and L.-A. Wu, "Nonlocal Talbot self-imaging with incoherent light," *Phys. Rev. A* **82**, 033803 (2010).
91. X.-B. Song, J. Xiong, X. Zhang, and K. Wang, "Second-order Talbot self-imaging with pseudothermal light," *Phys. Rev. A* **82**, 033823 (2010).
92. X.-B. Song, H.-B. Wang, J. Xiong, K. Wang, X. Zhang, K.-H. Luo, and L.-A. Wu, "Experimental observation of quantum Talbot effects," *Phys. Rev. Lett.* **107**, 033902 (2011).
93. J.-M. Wen, S. Du, H. Chen, and M. Xiao, "Electromagnetically induced Talbot effect," *Appl. Phys. Lett.* **98**, 081108 (2011).
94. H. Ling, Y. Li, and M. Xiao, "Electromagnetically induced grating: homogeneously broadened medium," *Phys. Rev. A* **57**, 1338–1344 (1998).
95. B. Erkman and J. H. Shapiro, "Ghost imaging: from quantum to classical to computational," *Adv. Opt. Photon.* **2**, 405–450 (2010).
96. T. B. Pittman, Y. H. Shih, D. V. Strekalov, and A. V. Sergienko, "Optical imaging by means of two-photon quantum entanglement," *Phys. Rev. A* **52**, R3429–R3432 (1995).
97. M. H. Rubin, "Transverse correlation in optical spontaneous parametric down-conversion," *Phys. Rev. A* **54**, 5349–5360 (1996).
98. J.-M. Wen, P. Xu, M. H. Rubin, and Y.-H. Shih, "Transverse correlations in triphoton entanglement: geometrical and physical optics," *Phys. Rev. A* **76**, 023828 (2007).
99. M. D'Angelo, M. V. Chekhova, and Y. H. Shih, "Two-photon diffraction and quantum lithography," *Phys. Rev. Lett.* **87**, 013602 (2001).
100. A. N. Boto, P. Kok, D. S. Abrams, S. L. Braunstein, C. P. Williams, and J. P. Dowling, "Quantum interferometric optical lithography: exploiting entanglement to beat the diffraction limit," *Phys. Rev. Lett.* **85**, 2733–2736 (2000).



**Jianming Wen** is Visiting Associate Professor and Visiting Scholar at the National Laboratory of Solid State Microstructures, Nanjing University, China. He obtained his Ph.D. in Physics from the University of Maryland, Baltimore County (UMBC), in 2007. Since then he has been a postdoctoral fellow at UMBC, the University of Virginia, the University of Arkansas, and the University of Calgary (Canada). He currently is a member of the Editorial Board of *Dataset Papers in Physics*. His research interests include quantum optics, quantum information, quantum memory, nonlinear optics, quantum imaging and lithography, cold atoms, superresolution imaging, and optomechanics.



**Yong Zhang** is an Associate Professor at the College of Engineering and Applied Sciences and National Laboratory of Solid State Microstructures, Nanjing University, China. He obtained his Ph.D. in Physics from Nanjing University, China, in 2007. He then spent two years as a postdoctoral fellow at the University of Arkansas. His research interests are in the areas of nonlinear optics, superresolution imaging, ultrafast optics, and quantum optics.



**Min Xiao** is a Professor at the School of Physics and National Laboratory of Solid State Microstructures, Nanjing University, China. He also holds an appointment (currently on leave) as Distinguished Professor of Physics and Endowed Chair in Nanotechnology at the Department of Physics, University of Arkansas, USA. He is a Fellow of the Optical Society of America and a Fellow of the American Physical Society. He currently serves as a Topical Editor for Journal of the Optical Society of America B. His research interests include quantum/nonlinear optics, atomic physics, optical properties of micro/nanostructures, and ultrafast spectroscopy. So far, he has published more than 270 refereed journal papers, which have had more than 6000 citations.